ONR-CR213-130-1F

INTRINSIC NOISE SOURCES IN VOLUME HOLOGRAPHY

W. J. Burke, P. Sheng, H. A. Weakliem
RCA LABORATORIES
Princeton, New Jersey 08540

DECEMBER 1975

FINAL REPORT
For the period 1 March 1975 to 31 October 1975

This research was sponsored by the Office of Naval Research under Contract N00014-75-C-0590.

Prepared for
OFFICE OF NAVAL RESEARCH
Department of the Navy
Arlington, Virginia 22217

UNCLASSIFIED

SECURITY CLASSIFICATION OF THIS PAGE (When Data Entered)

REPORT DOCUMENTATION PAGE

READ INSTRUCTIONS BEFORE COMPLETING FORM

1. REPORT NUMBER: ONR-CR213-130-1F
2. GOVT ACCESSION NO.:
3. RECIPIENT'S CATALOG NUMBER:

4. TITLE (and Subtitle): INTRINSIC NOISE SOURCES IN VOLUME HOLOGRAPHY

5. TYPE OF REPORT & PERIOD COVERED: Final Report. (3-1-75 to 10-31-75)

6. PERFORMING ORG. REPORT NUMBER: PRRL-75-CR-74

7. AUTHOR(s): W. J. Burke, P. Sheng, and H. A. Weakliem

8. CONTRACT OR GRANT NUMBER(s): N00014-75-C-0590

9. PERFORMING ORGANIZATION NAME AND ADDRESS:
RCA Laboratories
Princeton, N.J. 08540

10. PROGRAM ELEMENT, PROJECT, TASK AREA & WORK UNIT NUMBERS:

11. CONTROLLING OFFICE NAME AND ADDRESS:
Office of Naval Research
Department of the Navy
Arlington, Virginia 22217

12. REPORT DATE: December 1975

13. NUMBER OF PAGES: 68

14. MONITORING AGENCY NAME & ADDRESS (if different from Controlling Office):
65 p.

15. SECURITY CLASS. (of this report): Unclassified

15a. DECLASSIFICATION/DOWNGRADING SCHEDULE: N/A

16. DISTRIBUTION STATEMENT (of this Report)

Reproduction in whole or in part is permitted for any purpose of the U.S. Government.

Approved for public release; distribution unlimited.

17. DISTRIBUTION STATEMENT (of the abstract entered in Block 20, if different from Report)

18. SUPPLEMENTARY NOTES

19. KEY WORDS (Continue on reverse side if necessary and identify by block number)

Hologram
Volume holography
Holographic storing
Holographic fixing
Iron-doped $LiNbO_3$
Holographic signal-to-noise
Crosstalk
Intermodulation distortion

20. ABSTRACT (Continue on reverse side if necessary and identify by block number)

Noise sources intrinsic to volume phase holograms in iron-doped $LiNbO_3$ have been investigated. Intermodulation distortion, statistical noise, and scatter noise have been found to be insignificant. Crosstalk noise can be reduced to a level compatible with high-quality (S/N ratio ≥40 dB) readout images at angular spacings (0.1° in air) such that large numbers of holograms can be stored in a given volume.

DD FORM 1 JAN 73 1473

UNCLASSIFIED

SECURITY CLASSIFICATION OF THIS PAGE (When Data Entered)

299000 lb

20.

PREFACE

This report describes work performed during the period 1 March 1975 to 31 October 1975 in the Communications Research Laboratory of RCA Laboratories under Contract No. N00014-75-C-0590. Dr. K. Powers is the Laboratory Director and B. F. Williams is the Group Head. The Project Scientist is W. J. Burke. P. Sheng and H. A. Weakliem participated in the research.

The Government Project Monitor is Cmdr. D. Hanson.

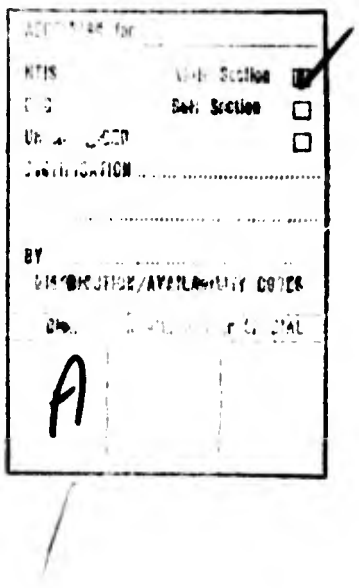

TABLE OF CONTENTS

LIST OF ILLUSTRATIONS

LIST OF ILLUSTRATIONS (Continued)

I. INTRODUCTION

The information storage capacity of volume holography is extremely large. Van Heerden [1] has shown that the capacity of volume holograms is $\sim(xyz)/\lambda^3$ where x,y,z are the dimensions of the holograms. Accessing of this information is made possible by the Bragg condition on constructive interference of light scattered from different portions of the holographic grating. This condition permits constructive interference of the light scattered from a particular hologram to occur only for a limited range of wavelengths or angles of incidence of the readout beam. These considerations lead to theoretical storage densities of $\sim 8 \times 10^{12}$ elements/cm^3. In practice, this theoretical limit cannot be attained because of the physical limitations of the recording and readout systems, sample geometry, and signal-to-noise considerations. This approach is, however, still an extremely attractive one because of the large storage capacity coupled with ease of readout (simply changing the angle of incidence of the readout beam on the storage medium).

The applicability of this technique has been limited, until recently, by the lack of a storage medium in which large numbers of high efficiency thick-phase holograms could be recorded and fixed with reasonable efficiency. Research at RCA Laboratories, with Navy support, has led to the development of iron-doped $LiNbO_3$ as a thick phase storage material for application to a moving map display [2,3,4]. This material has excellent optical quality, high sensitivity for recording holograms, and the capability of fixing these holograms.

The mechanism by which holograms are recorded and fixed in iron-doped $LiNbO_3$ is the following. Iron ions, present in the 2+ and 3+ valence states, photosensitize $LiNbO_3$. Absorption of light by Fe^{2+} ions generates free electrons which can be trapped at Fe^{3+} sites. Phase holograms are recorded by photo-excitation of electrons trapped at Fe^{3+} sites with subsequent drift or

1. P. J. Van Heerden, Appl. Optics 2, 393 (1963).
2. D. L. Staebler, W. Phillips, and B. W. Faughnan, *Materials for Phase Holographic Storage (U)*, Final Report, Contract N00019-72-C-0147, March 1973.
3. D. L. Staebler, W. Phillips, W. Burke and B. W. Faughnan, *Materials for Phase Holographic Storage*, Final Report, Contract No. N00019-73-C-0273, February 1974.
4. W. J. Burke, W. Phillips, D. L. Staebler, and B. F. Williams, *Materials for Phase Holographic Storage*, Final Report, Contract No. N00019-74-C-0312, April 1975.

diffusion of the electrons from regions of high light intensity in the interference pattern of the light beams into regions of lower light intensity and retrapping at Fe^{3+} ions. Through this process, a trapped electronic space charge pattern is formed which mirrors the original light intensity pattern. This space charge pattern modulates the index of refraction through the electro-optic effect producing the phase grating [5,6,7,8].

Heating the crystal in which the hologram is stored, to between 100° and 200°C, produces a transport of an ionic species which neutralizes the electronic space charge pattern [9,10]. Upon cooling to room temperature and redistributing the electronic space charge pattern with incoherent light, a hologram due to the ionic space charge pattern, remains. We have found also that the two processes of recording and fixing the holograms can be carried out simultaneously by recording the holograms with the crystal held at 160°C (write-while-hot technique).

The exact nature of this ionic species is, at present, unknown. Silicon has, however, been recently identified as a mobile ion in $LiNbO_3$ [4,11]. If silicon is, in fact, the mobile fixing ion, then an increase in the silicon concentration could lead to lower fixing temperatures, thus reducing the thermal erasure during recording.

We have recorded and fixed over 500 holograms in iron-doped $LiNbO_3$, using the technique described above, each hologram having a diffraction efficiency greater than 2.5% [4,12]. From these results, as well as investigations of

5. J. J. Amodei, W. Phillips, and D. Staebler, IEEE J. Quantum Electron. QE-7, 63 (1971).
6. G. E. Peterson, A. M. Glass, and T. J. Negran, Appl. Phys Lett. 19, 130 (1971).
7. F. S. Chen, J. T. LaMacchia, and D. B. Frazer, Appl. Phys. Lett. 13, 233 (1968).
8. D. L. Staebler and J. J. Amodei, J. Appl. Phys. 43, 1042 (1972).
9. J. J. Amodei and D. L. Staebler, Appl. Phys. Lett. 18, 540 (1971).
10. D. L. Staebler and J. J. Amodei, Ferroelectrics 3, 107 (1972).
11. B. F. Williams, W. J. Burke and D. L. Staebler, Appl. Phys Lett., to be published.
12. D. L. Staebler, W. J. Burke, W. Phillips, and J. J. Amodei, Appl. Phys. Lett. 4, 182 (1975).

other dopants in $LiNbO_3$ and a comparison with other recording materials, we have concluded that iron-doped $LiNbO_3$ is the best volume holographic storage medium available at the present time [4].

The ultimate storage capacity of iron-doped $LiNbO_3$ will be limited by the required S/N ratio in the readout image. Holographic noise sources have been extensively studied for the case of thin phase and absorption holograms [13,14,15,16]. The noise sources present in thin-phase holograms are scattering from defects in recording material and intermodulation distortion. Intermodulation distortion arises from nonlinearities in the recording sensitivity and in the recording process itself. Either or both of these processes can produce an interference pattern of the object beam with itself. This interference gives rise to a low-frequency grating from which the reconstructed object beam is diffracted, giving rise to multiple ghost images of the object [16].

These noise sources are intrinsic to the recording material and/or the recording process. Because coherent light is used in the recording process the readout image is also extremely susceptible to degration due to light scattering from defects such as dust and scratches in the optical system, and from multiple reflections. Gerritsen et al. [14] have shown that the use of multiple object beam illumination can significantly reduce the magnitude of this effect. The extent of the improvement is limited, however, since in the limit of diffuse illumination the image is dominated by speckle noise. The use of multiple object beam illumination to reduce cosmetic noise in volume phase holograms in iron-doped $LiNbO_3$ has been studied. The results show that the S/N ratio improvements noted for thin-phase holograms also occur for volume holograms.

The sources of intrinsic noise in volume holography have been investigated by several workers. Baugh [17] has investigated the properties of volume holograms of complex objects, including signal distortion and nonlinearities.

---

13. D. H. R. Vilkomerson, "A Holographic Communication Theory," Ph.D. Thesis, Columbia University (1969).
14. H. J. Gerritsen, W. J. Hannan, and E. G. Ramberg, Appl. Opt. 7, 2301 (1968).
15. E. G. Ramberg, RCA Review 33, 5 (1972).
16. R. A. Bartolini, Applied Optics 13, 129 (1974).
17. R. Baugh, "High Efficiency Volume Holography," Ph.D. Thesis, Stanford University (1969).

Zech [18] has studied various aspects of digital data storage in organic media using volume holography. His work included studies of material nonlinearities, nonlinear noise sources, and crosstalk. These studies were carried out on samples less than 0.1 cm thick. The results of this work will be compared with our work.

Ramberg [15] has considered the noise sources present in volume holographic storage. Assuming single scattering of the reconstruction beam he has calculated the S/N ratio expected for crosstalk between holograms stored at different angles of incidence of the reference beam. The noise contribution arising from statistical fluctuations in the location of trapped electrons forming the grating was also calculated. Ramberg's calculations predict a serious limitation on the number of holograms which can be stored in iron-doped $LiNbO_3$ at a reasonable S/N ratio.

In this report we shall present the results of a study of three *intrinsic* sources of noise in a volume hologram. These are the crosstalk between holograms, intermodulation distortion arising from material and recording nonlinearities, and statistical noise. We do not include in this work noise arising from spurious light-induced scattering during hologram reconstruction since this has been covered in earlier work [20]. We have also not included in this study any work on cosmetic noise arising from defects or reflections in the optical system, since these effects are dealt with in a recent report, and the method of treating them is identical to that for thin holograms [19].

The remainder of this report is organized into five sections. Section II covers sample preparation, the measurement apparatus, and the definition of noise used here. Sections III, IV, and V cover our studies on crosstalk, intermodulation distortion, and statistical noise, respectively. Section VI contains the summary and conclusions of these studies.

---

18. R. G. Zech, "Data Storage in Volume Holograms," Ph.D. Thesis, University of Michigan (1974).
19. G. A. Alphonse and W. Phillips, Final Report, Contract No. NAS8-26808, National Aeronautics and Space Administration, May 1975.
20. W. J. Burke, *S/N Ratio of Holographic Images*, Final Report, Contract No. N00019-75-C-0494, November 1975.

II. EXPERIMENTAL METHODS

A. CRYSTALS

Poled single crystals of $LiNbO_3$ containing 0.01 to 0.05 mole % Fe, grown by the Crystal Technology Corp., were used in these studies. The crystals were oxidized by W. Phillips of RCA Laboratories in an Ar + O_2 atmosphere at 950°C for 24 hours to obtain the desired optical density (0.2 to 0.3 at 488.0 nm) [4,21]. The oxygen content of the atmosphere is varied, depending upon the iron-dopant concentration and the crystal thickness, to obtain the desired optical density. Figures 1 and 2 show the optical density and the calculated absorption constant as a function of wavelength for light polarized parallel to the c-axis of the crystal as measured on a Cary 14 spectrophotometer. The broad absorption for wavelengths greater than 400 nm is due to the fraction of the iron dopant in the 2+ valence state.

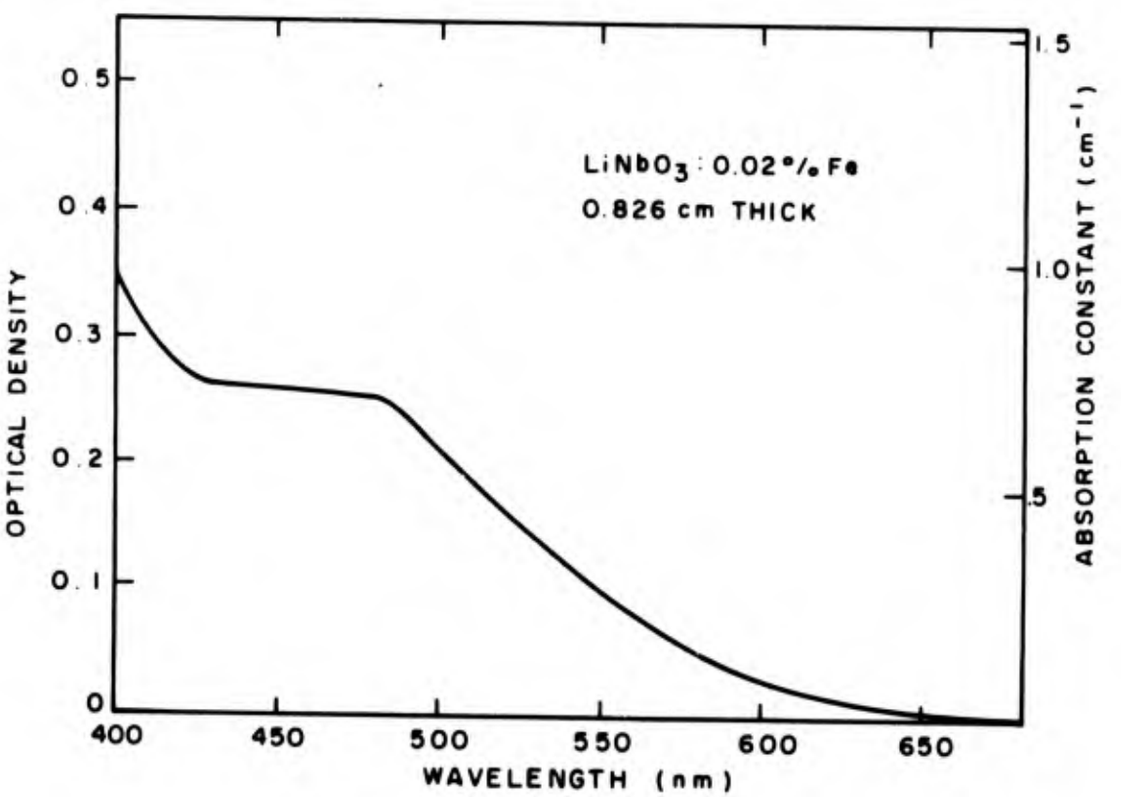

Figure 1. Optical absorption spectrum of a 0.826-cm-thick crystal of 0.02 mole % Fe-doped $LiNbO_3$.

21. W. Phillips and D. L. Staebler, J. Elect. Materials 3, 601 (1974).

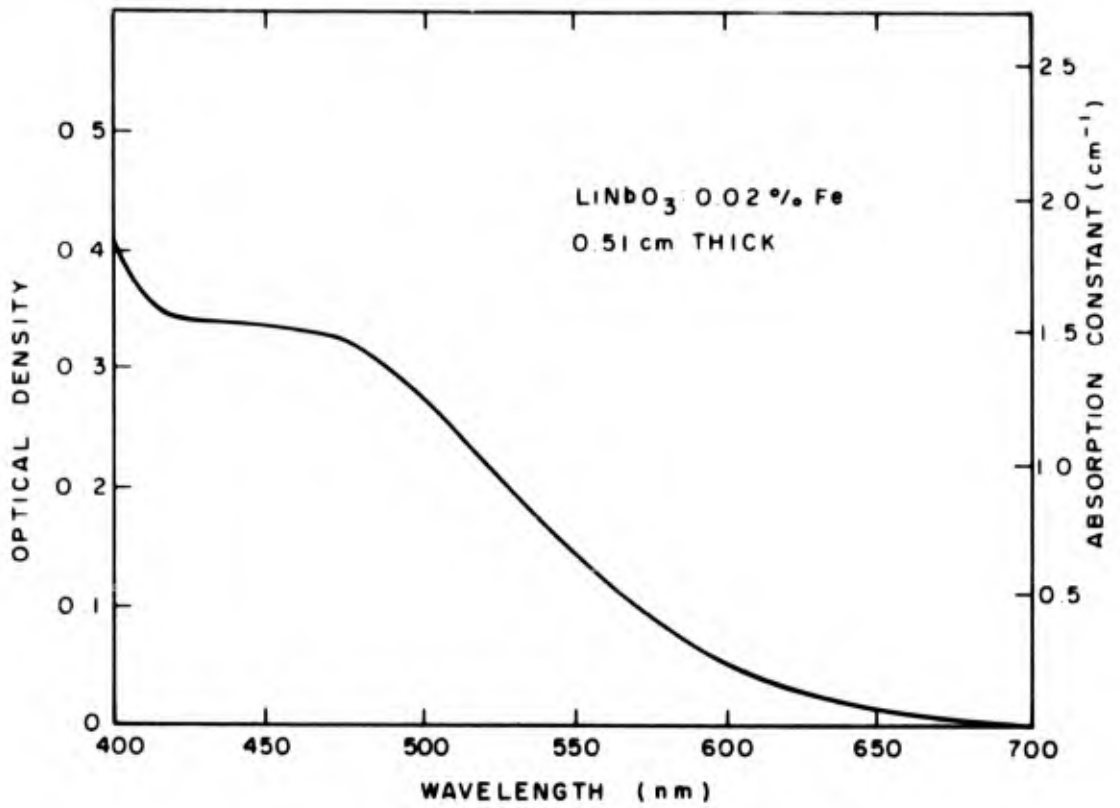

Figure 2. Optical absorption spectrum of a 0.51-cm-thick crystal of 0.02 mole % Fe-doped $LiNbO_3$.

After the oxidation treatments and rough surface polishing, the crystals were repolished using a SYTON chemical polish to reduce surface scattering. Light scattered from these crystals at an angle of 30° (which is the angular separation of the object and reference beams) was measured to be typically on the order of ∿100 dB (see Part C. below) down from the incident light beam intensity at 488 nm. The sources of this light scattering include surface scratches, pits, etc., left from the polishing procedure, dust on the surface, and bulk imperfections. The bulk imperfections include cracks, voids, index of refraction variations due to local variations in the crystal composition induced during growth, and small volumes of reversed domains reported earlier [4].

The crystals were then carefully cleaned and the large faces coated with a single layer of evaporated SiO_2 ∿825 Å thick by D. Hoffman of RCA Laboratories. This thickness of SiO_2 produced an antireflection coating on the crystal which reduced the surface reflections from ∿20% to ∿2% at each face. These coatings were found to be of good optical quality, and stable under repeated cycling

to ∿250°C during the write-while-hot recording procedure and during subsequent heating to erase the fixed holograms. This decrease in reflection from the crystal surfaces had two important results:

(1) Interference beats in the readout image resulting from multiple reflections at the crystal surfaces were significantly reduced.

(b) Light reflected from the crystal and scattered from the different optical components are collected by the imaging optics and counted as a noise source. This source of noise is significantly reduced by the decrease in the reflected light.

In the work reported here, crystal thickness varied from 0.04 to 1 cm.

B. RECORDING APPARATUS

Holograms were recorded using an Ar^+ ion laser operating in the TEM_{00} mode at 488.0 nm. Since several different experimental arrangements were used for the studies reported here, schematic diagrams of the recording apparatus are shown in the different sections of this report. The features of the apparatus common to the different experiments were the laser, dielectric beam splitter, and beam expanders with spatial filters in both the object and reference beams, to reduce or remove nonuniformities in the beams due to light scattering and multiple reflections in the preceding portions of the optical system.

C. NOISE MEASUREMENTS AND DEFINITION

Noise measurements were made using an RCA 931A photomultiplier in either a fixed position or as it scanned across the readout image. The particular arrangement depended upon the type of measurement being made.

For the measurements reported here, the S/N ratio is defined as the ratio of the signal to the background noise level due to the effect under investigation. For the photomultiplier tube, the output current is proportional to the incident light intensity. The S/N ratio (SNR) expressed in dB is:

$$SNR = 20 \log \left(\frac{I}{I_n}\right) = 20 \log \left(\frac{i}{i_n}\right) \qquad (1)$$

where I is the signal light intensity, I_n is the noise light intensity, i is the signal output current from the photomultiplier tube, and i_n is the noise output current. The television engineer defines SNR in terms of the rms value of the noise fluctuations. Here we choose to use what is, in effect, a peak-to-peak value of the noise, since what is measured is not the fluctuation in intensity across the image, but light scattered into the image due to one or more of the noise mechanisms under study. This light does not appear as a fluctuation in intensity, but as an additional dc signal component. The definition in terms of rms values add ∿9 dB to the S/N ratio quoted here.

III. CROSSTALK

Holograms are recorded in iron-doped $LiNbO_3$ as a modulation of the index of refraction. Reconstruction of the original object wavefront can occur at or near the Bragg condition for constructive interference of light scattered from different parts of the grating. The Bragg condition limits the range of angles of incidence or wavelengths of the readout light beam. This selectivity on readout angle or wavelength provides a method for multiple storage of holograms in the same volume. Angular selectivity is most commonly used for multiple storage since the variation in angle can be easily obtained by rotation of the storage medium or by deflection of the laser beam. Variation of wavelength is not a practical approach because of the broad range of wavelengths of coherent light required for the storage of large numbers of holograms ($\sim$319 Å/degree of angular spacing at 488 nm). This approach has been used, however, for the direct recording of color objects using the blue, green, and red output from a mixed Ar^+/Kr^+ ion laser [22,23]. Another method used has been to rotate the crystal about an axis perpendicular to the surface of the storage medium and lying in the recording plane, as opposed to rotation about an axis perpendicular to the recording plane. This approach, known as spatial frequency multiplexing [18], is not adaptable to electro-optic materials such as $LiNbO_3$, due to their anisotropy.

A. THEORY

The simplest approach, then, is angular multiplexing of the holograms with rotation of the storage medium about the axis perpendicular to the recording plane. Kogelnik [24] has calculated the angular and wavelength sensitivity, using coupled wave theory, and has obtained expressions for the diffraction efficiency as a function of angular and/or wavelength change. For

22. J. J. Amodei, W. J. Burke, and D. L. Staebler, *Volume Holographic Materials Characterization and Device Feasibility for Map Display Applications*, Final Report, Contract No. N62269-71-C-0533, July 1972.
23. W. Burke and D. L. Staebler, *Volume Holographic Material Device Feasibility for Map Display Applications*, Final Report, Contract No. N62269-72-C-0793, June 1973.
24. H. Kogelnik, Bell Syst. Tech. J. 48, 2909 (1969).

a thick-phase grating in an absorptive medium, Kogelnik [24] calculated the diffraction efficiency η to be:

$$\eta = e^{-D_o(1 + c)} \sin^2 (\nu^2 + \xi^2)^{1/2}/(1 + \xi^2/\nu^2) \tag{2}$$

where $D_o = \alpha\ell/\cos \theta_R$

α = absorption constant

ℓ = crystal thickness

θ_R = the angle of incidence of the reference beam in the crystal

$C = \cos \theta_R/\cos \theta_o$

θ_o = the angle of incidence of the object beam in the crystal

$$\nu = \pi\Delta n\ell/\lambda \sqrt{\cos \theta_R \cos \theta_o} \tag{3}$$

Δn is the peak modulation of the index of refraction

$$\xi^2 = \frac{\Theta^2 \ell^2}{4 \cos^2 \theta_o} - \frac{D_o^2 (1 - c)^2}{4} \tag{4}$$

$$\Theta^2 = \frac{4\pi n\Delta\theta}{\lambda} \cos (\phi - \theta_R) \sin (\phi - \theta_R) \tag{5}$$

n is the index of refraction

$\Delta\theta$ is the angular deviation from the Bragg condition in the crystal

ϕ is the slant angle of the grating in the crystal.

Figure 3 shows a plot of the diffraction efficiency η calculated from Eq. (2) vs the angular deviation measured in air of the readout beam from the Bragg condition. This curve was calculated for a 10% peak diffraction efficiency hologram in a 0.826-cm-thick crystal with an optical density of 0.25. Figure 4 shows the diffraction efficiency ratio plotted in dB [20 $\log \eta_{MAX}/\eta(\Delta\theta)$]. From these curves it is clear that the diffraction efficiency rolls off rapidly with angular deviation from the Bragg angle, and that a definite periodicity exists in the oscillation of the side lobes. This period is 15 milli-degrees

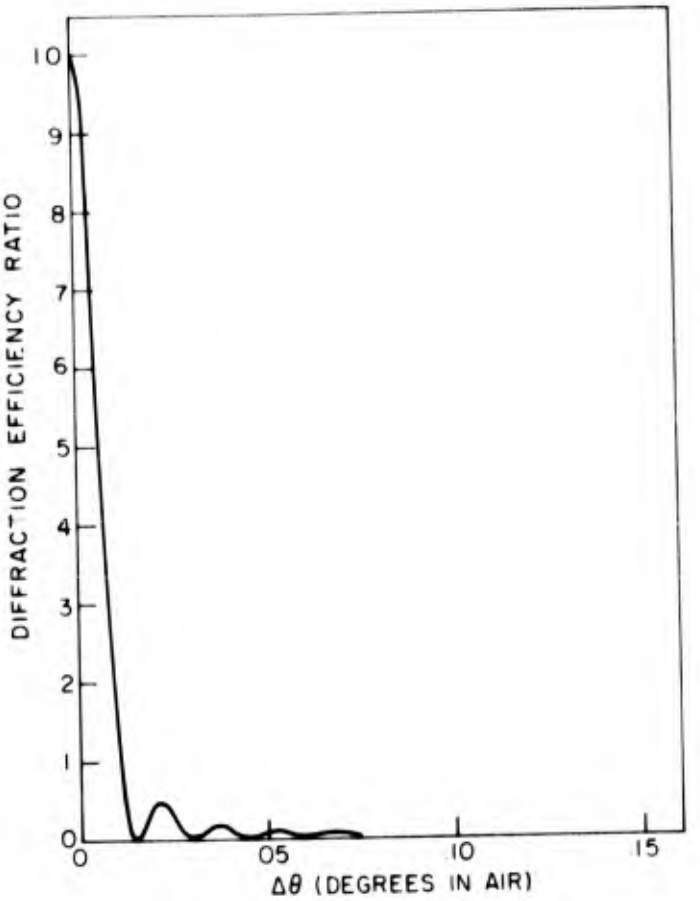

Figure 3. Diffraction efficiency ratio vs the angular deviation of the readout beam from the Bragg condition as measured in air for a 0.826-cm-thick crystal of $LiNbO_3$.

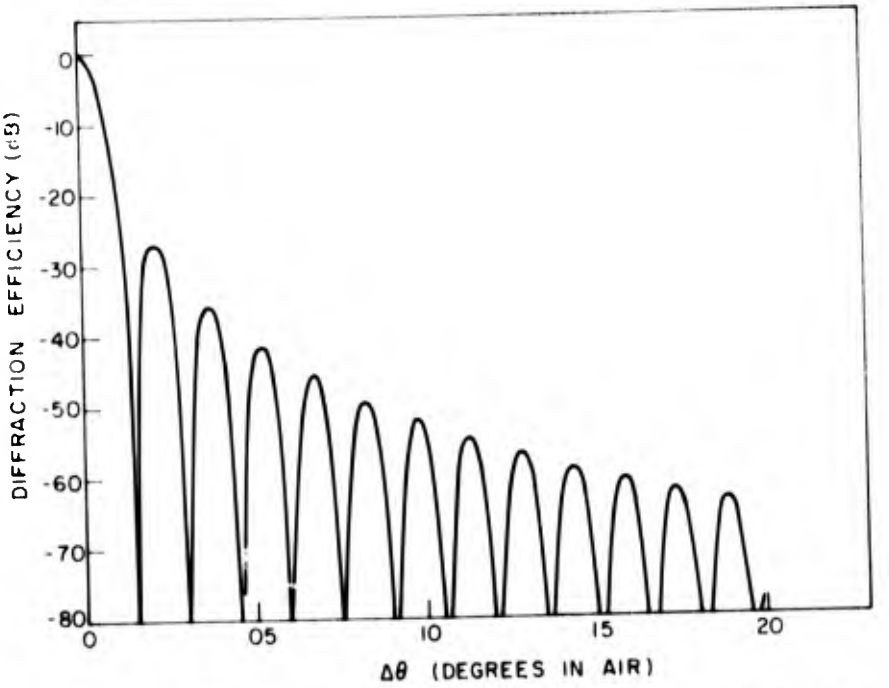

Figure 4. Same as Fig. 3 with the diffraction efficiency ratio plotted in dB.

in air for a 0.826-cm-thick crystal, and is related to the crystal thickness d by

$$\Delta\theta_{air} \approx \frac{2n\lambda}{d} \tag{6}$$

The envelope of the rolloff in efficiency is of the form $\frac{\sin^2 x}{x^2}$ since for $\Delta\theta > 0$, ν^2 is a constant and ξ^2 rapidly becomes much larger than ν^2.

For maximum packing of holograms, the angular spacing between holograms should be as small as possible. The limiting constraint on the packing density will be the acceptable S/N ratio in a readout image. The noise in this case is the crosstalk from all other holograms stored in the crystal. The problem is to measure the crosstalk noise as a function of the angular separation between holograms and as a function of the number of holograms stored.

B. MEASUREMENTS

The experimental arrangement used to measure the crosstalk noise is shown in Fig. 5. The crystal was mounted in a vise on the stepping motor and the

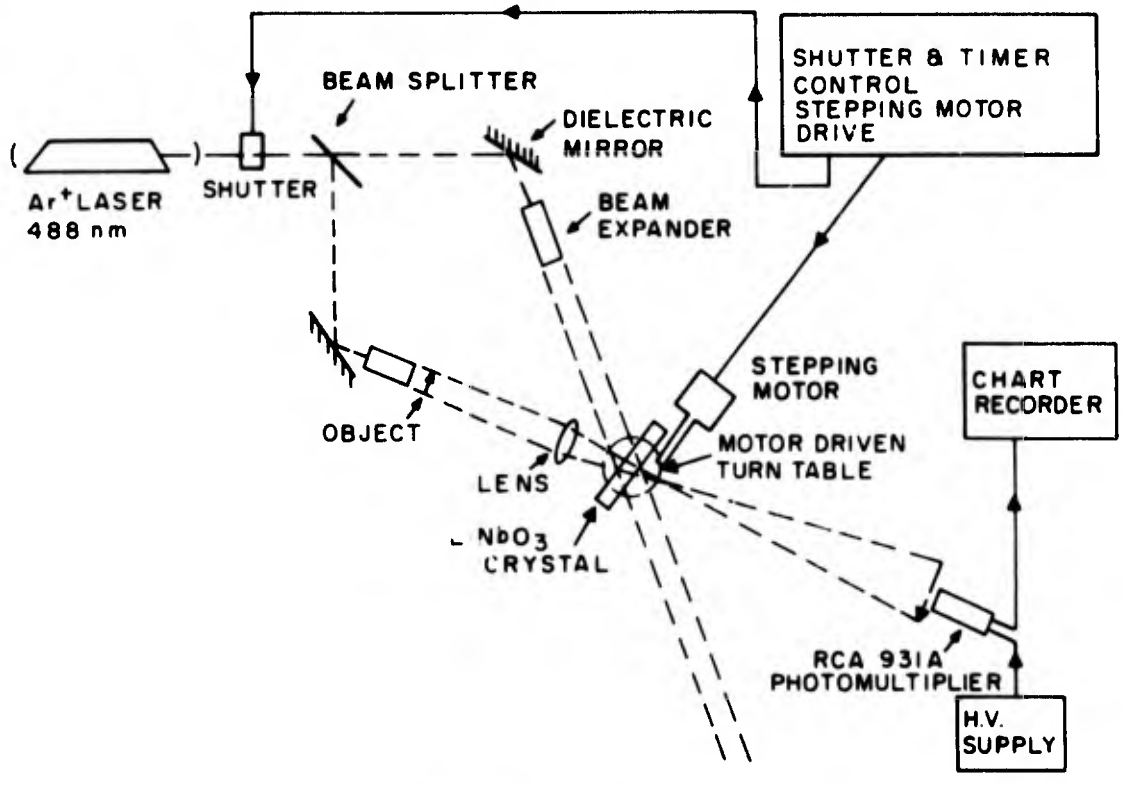

Figure 5. Experimental apparatus used to measure hologram crosstalk.

holograms sequentially recorded. The stepping motor automatically advanced a fixed amount after each hologram was recorded, and was measured to have a cumulative accuracy of ∿0.1% over a large number of small (0.02°) steps. The accuracy of individual steps of this size was not measured.

Holograms of the bar pattern shown in Fig. 6(a) were recorded with a diffraction efficiency ∿10% at angular positions which were multiples of the fixed step. In the measurements to be presented here, 50 holograms were recorded with a fixed angular spacing ranging from 0.04 to 0.20° between them. To measure the crosstalk, 25 holograms were recorded, an angular position left blank, and 25 more holograms were recorded. The recorded holograms were then read out sequentially by rotating the crystal at a uniform rate. The readout image was detected with an RCA 931A photomultiplier tube and displayed on a chart recorder. The signal level was the average value of the intensity of the light diffracted on a small fraction of the center of the image. The noise level was the value of the light intensity at the position of the missing hologram.

The object transparency used for these measurements shown in Fig. 6(a) was a 10-mm-wide frame on 16-mm film. A similar transparency with the central bar missing, as shown in Fig. 6(b), was used to determine the background scattering in the object transparency, optics, and crystal. The ratio at the center of the middle bar of this pattern for the bar/no bar case was ∿95 dB. Therefore, the background scattering is negligible.

The 50 holograms recorded for each angular spacing were of approximately equal intensity. This was accomplished by compensating for the optical erasure of the first holograms recorded by using successively shorter exposures as the holograms are recorded. The exposure time t_j for the jth hologram in a sequence was calculated from the exposure time t_o for the first hologram in the sequence using the relation [2]

$$t_j = t_o \left(\frac{\beta}{\beta + j - 1} \right) \tag{7}$$

where β is the erase/ record asymmetry. For the crystals used in these experiments, β ≈ 50 was found to produce holograms of approximately equal efficiency. Two distinct types of fluctuations were observed in the peak diffraction efficiency. The first would produce a single hologram whose efficiency was ∿50%

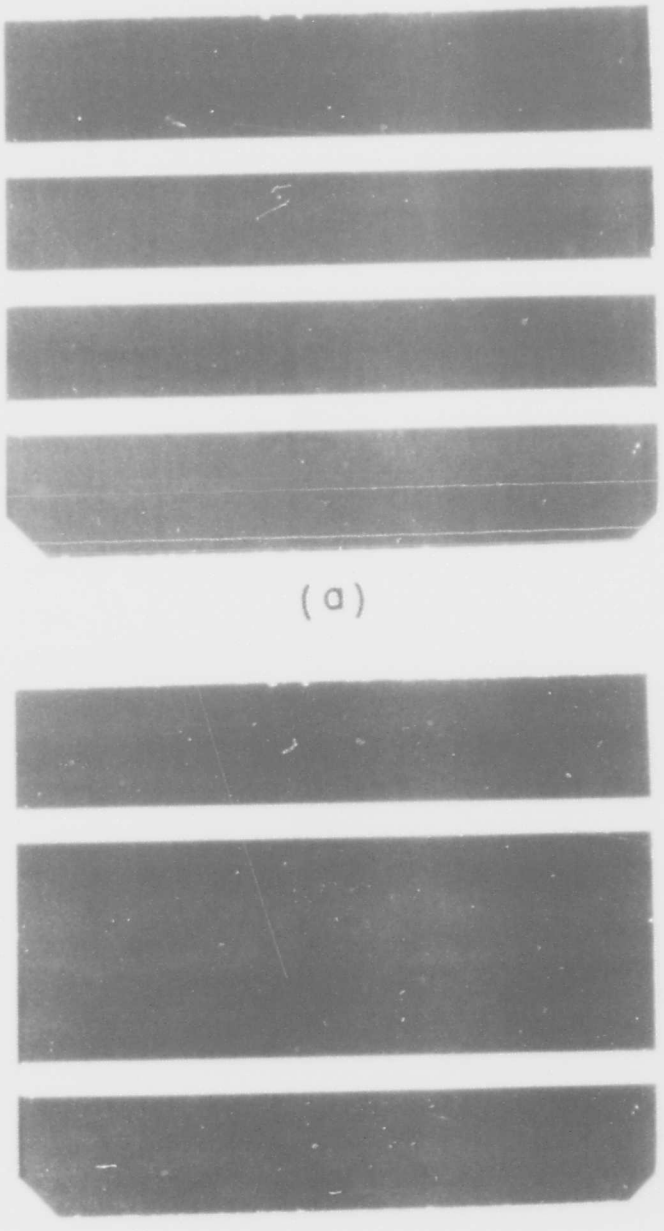

Figure 6. Photograph of (a) bar pattern on a 16-mm transparency; (b) bar pattern on a 16-mm transparency with central bar missing.

of the average efficiency, due most likely, to vibrations in the recording apparatus. The second was an oscillatory variation in peak efficiency whose period was ∿1/3 of the total number of holograms; due most likely to wandering of the recording beams arising from instabilities in the laser. The amplitude of this effect was ∿1/3 of the peak efficiency.

The results of measurements on 0.826- and 0.51-cm-thick samples are shown in Figs. 7 and 8, respectively. The spacing of the data points on these curves corresponds to the minimum increment in angular spacing possible with the stepping motor controller. The S/N ratio at large angular spacing (>0.1°) exhibits an oscillatory behavior with a period of ∿0.02° for the 0.826-cm-thick sample, and ∿0.03° for the 0.51-cm-thick sample.

The solid lines on each of these plots indicate the S/N ratio calculated from Eq. (2), assuming that the light diffracted from each of the holographic gratings recorded in the crystal in the off-Bragg condition adds incoherently to form the crosstalk noise at the readout image. The curves presented have a broadening or averaging added to account for slight variations in angle. The averaging consists of using the mean noise calculated for the angle of interest and for the angular positions ±0.001° and ±0.002°. The effect of this averaging is to reduce the extremely sharp peaks (∿0.002°) in the S/N ratio, but not affect the lower bound of the oscillation.

The origin of the oscillatory behavior is evident from Fig. 4. The period of the calculated S/N ratio oscillations shown in Fig. 4 corresponds exactly to the period of the oscillations in the side lobes of the angular dependence for the single hologram.

The most interesting point of the comparison of the theory and experiment is, however, the fact that the period of the theoretical and experimental oscillations differs significantly. The measured period is ∿30% larger for the 0.826-cm-thick crystal, and ∿20% larger for the 0.51-cm-thick crystal.

The correlation between the period of the minima in the side lobes of a single hologram and the period of the maxima in the calculated S/N ratio indicates that the apparent crystal thickness is less than the actual thickness. A fit to the period of oscillation of the data was obtained, using a crystal thickness of 0.625 cm for the 0.826-cm crystal, and 0.45 cm for the 0.51-cm crystal. The results of these calculations are plotted in Figs. 9 and 10.

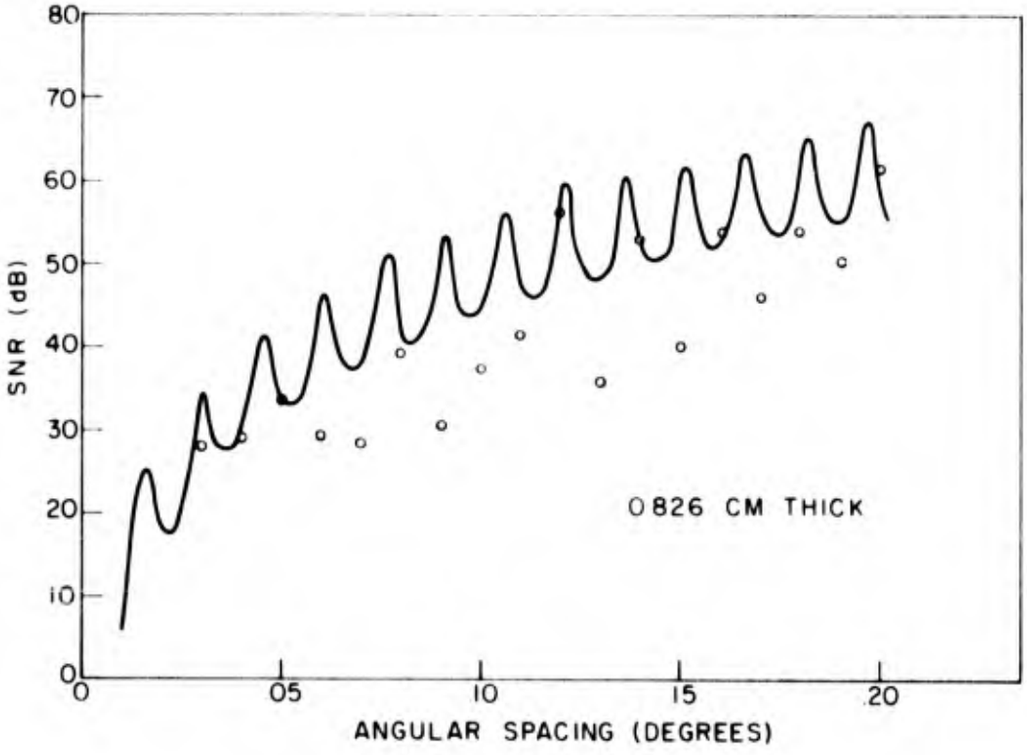

Figure 7. Measured S/N ratio as a function of angular spacing in air between holograms for a 0.826-cm-thick crystal. The solid curve is calculated from Eq. (1) for a grating thickness of 0.826 cm.

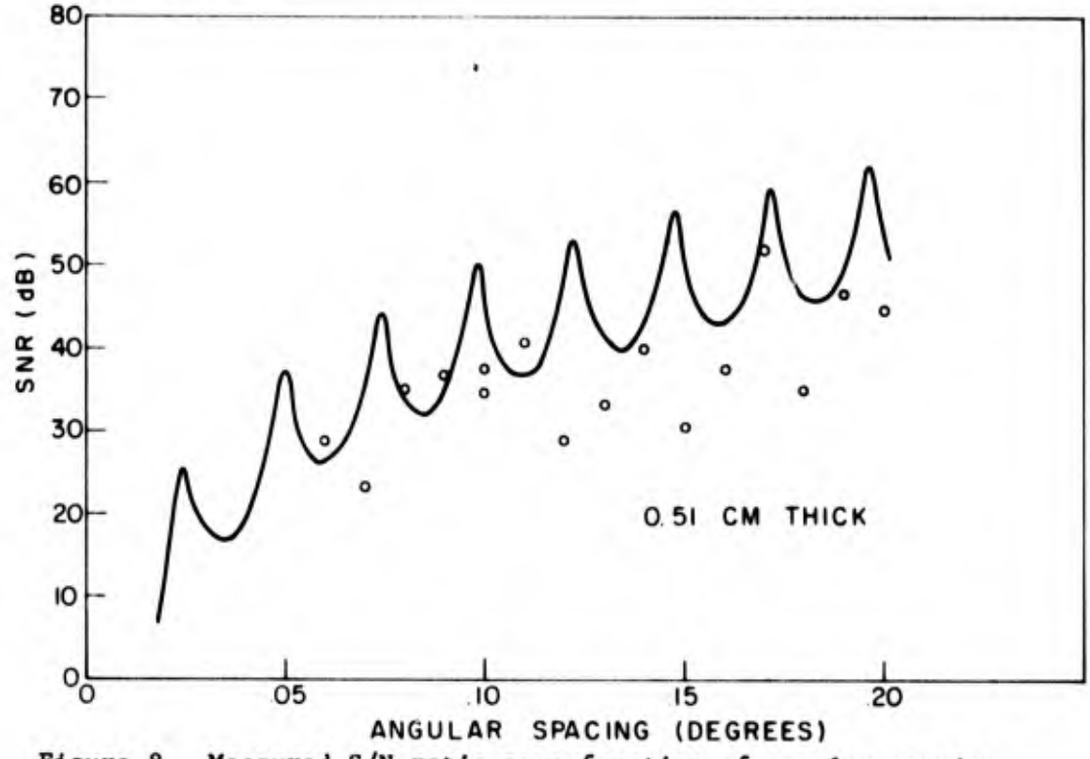

Figure 8. Measured S/N ratio as a function of angular spacing in air between holograms for a 0.51-cm-thick crystal. The solid curve is calculated from Eq. (1) for a grating thickness of 0.51 cm.

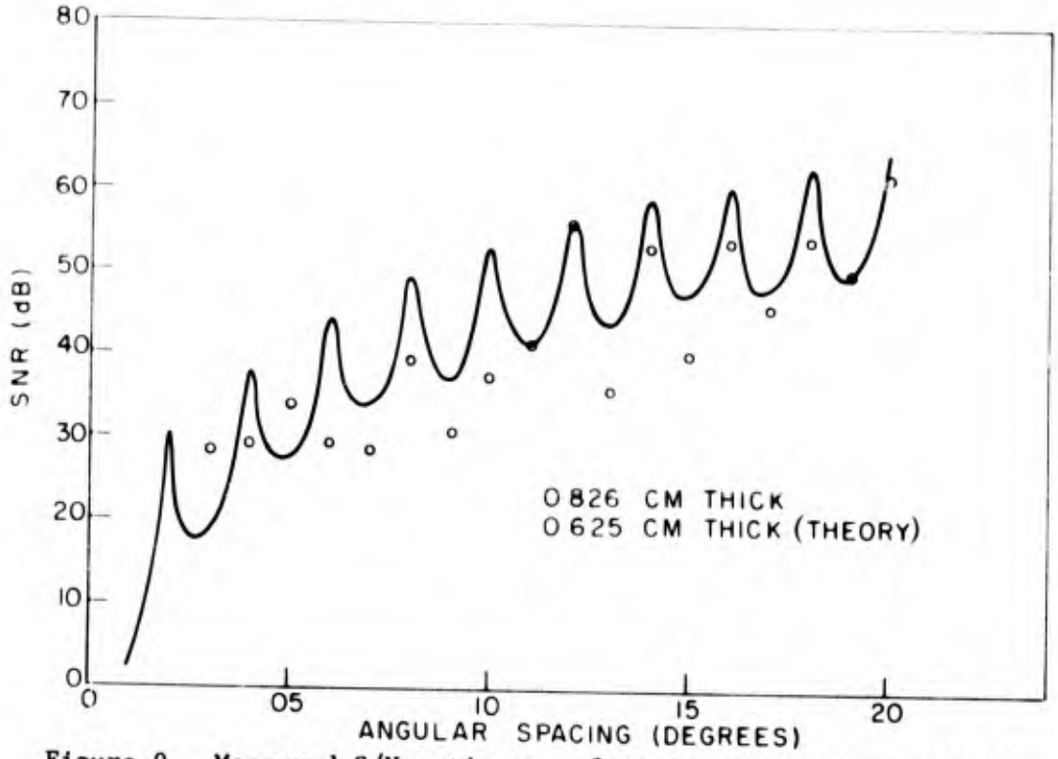

Figure 9. Measured S/N ratio as a function of angular spacing in air between holograms for a 0.826-cm-thick crystal. The solid curve was calculated from Eq. (1) for a grating thickness of 0.625 cm.

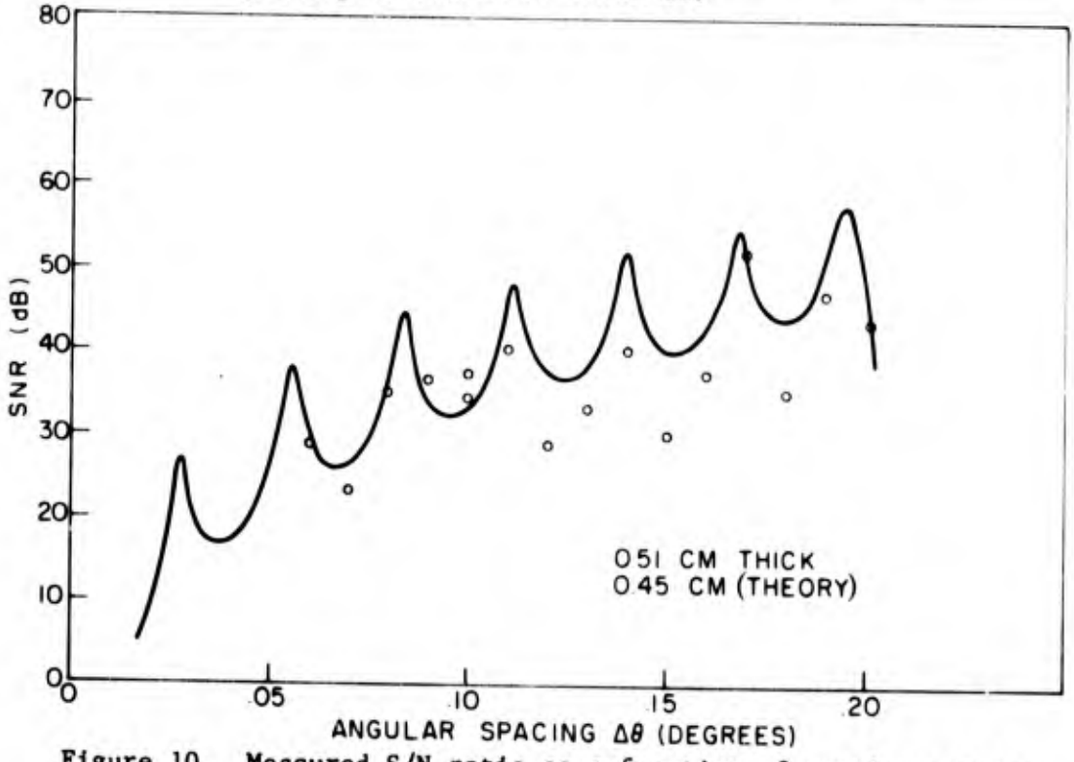

Figure 10. Measured S/N ratio as a function of angular spacing in air between holograms for a 0.51-cm-thick crystal. The solid curve is calculated from Eq. (1) for a grating thickness of 0.45 cm.

For the 0.826-cm crystal, the fit to the data is quite good; the reduced thickness predicts both the period and the location of the maxima quite accurately. For the 0.51-cm crystal, the fit is not quite as good, but it is still indicative that the apparent thickness is less than the actual thickness.

The origin of this effect may lie in the fact that the amplitude of the holographic grating is not uniform through the thickness of the crystal. The major contribution to the reconstructed object beam is due to only a portion of the crystal, with the remainder contributing only a small fraction of the scattered amplitude. There are two possible reasons for a grating thickness less than the crystal thickness:

(1) A grating is formed only in those volumes of the crystal where the two recording beams overlap. If they do not overlap, then no grating is formed in that portion of the crystal thickness, and the grating will be thinner than the crystal thickness. Figure 11 is a scale drawing of the

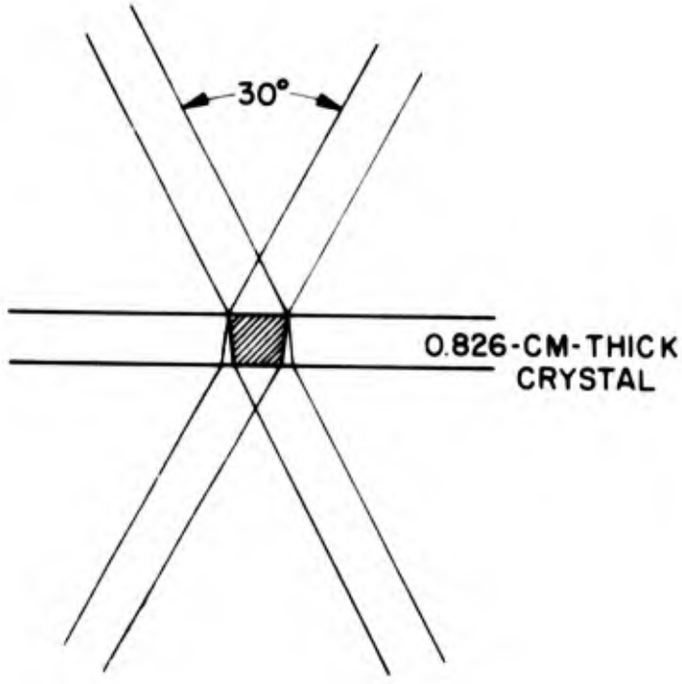

Figure 11. Scale drawing of the overlap of two beams separated by 30° in air in a 0.826-cm-thick crystal of $LiNbO_3$.

beam positions and overlap for this experiment. The large index of refraction of $LiNbO_3$ produces a strong refraction of the beams at the crystal surfaces, which tends to keep the beams together as they pass through the crystal. As seen in Fig. 11, there is only a ∿20% narrowing of the region of overlap from front to back. This is consistent with our visual observation of the beam overlap at the front and back crystal faces. In our experiments, it does not appear likely that poor beam overlap is contributing to the thin grating effect.

(2) The index of refraction modulation is directly proportional to the light intensity I, which is attenuated in transit through the crystal. The grating amplitude, then, decreases from the front to the back face of the crystal. This is shown in Fig. 12 for a 0.826-cm-thick crystal with an optical density of 0.25. The contribution to the scattered intensity from the back portion of the crystal will be significantly less than from the front, and the grating will appear to be thinner.

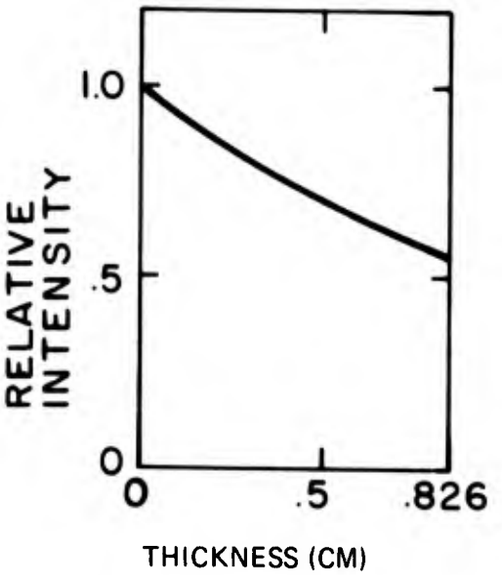

Figure 12. Light intensity as a function of crystal thickness for a 0.826-cm-thick crystal with an optical density of 0.25 at 488.0 nm.

This effect, as in (1) above, will also cause a difference between the theoretical and measured locations of the sidelobes of a single hologram. Measuring the locations of the sidelobes with a rotating turntable, we found the positions of the sidelobes to be positioned as predicted by the theory for

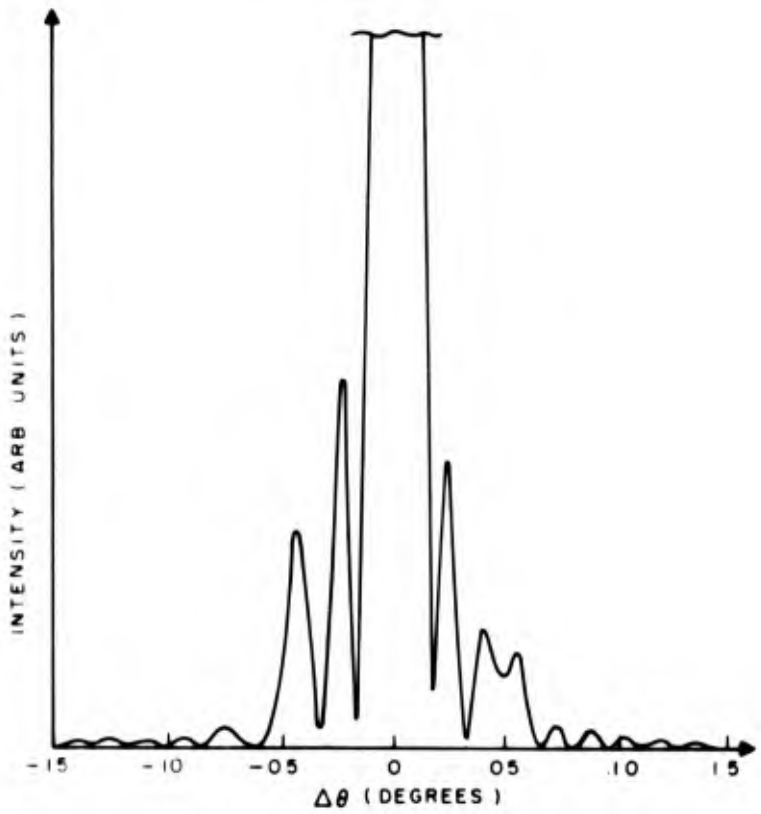

Figure 12. Measured diffracted light intensity as a function of angular deviation from the Bragg condition as measured in air for a 0.826-cm-thick crystal.

the actual thickness of the crystal within the accuracy of our measurement. This is shown in Fig. 13. If the grating were effectively thinner than the crystal, then the spacing of the sidelobes should increase. Zech [18] has observed the spacing of the sidelobes in a sample of polymethyl methacrylate to be ∿20% greater than predicted by theory. He hypothesized that this was due to nonuniform absorption in the sample. In our case, the measured value was in agreement with the theory.

The reason for this discrepancy is unclear at this point. The crosstalk measurements indicate that the grating is thinner than the crystal. Measurements on single holograms indicate that the grating thickness is approximately equal to the crystal thickness. The fit to the oscillations obtained by using the coupled wave theory indicates that the modification lies in the grating thickness.

C. DISCUSSION

The measured S/N ratio as shown in Figs. 9 and 10 is lower than that calculated from the coupled wave theory using either the true or effective crystal thickness. The theoretical curves shown in these figures include a broadening effect introduced by averaging the noise over a range of ±0.002°. This averaging has the effect of reducing the peaks in the S/N ratio, while leaving the minima, which are much broader, unaffected. The measured minima are 5 to 10 dB lower than the theory predicts. At smaller angular spacing the S/N ratio is approximately constant. This is due to a combination of several factors: the limited angular resolution of the stepping motor during readout, the smearing in angular position of the holograms, due to the light-induced change in the dc index of refraction, and the difficulty in measuring the magnitude of the noise when the holograms are so closely packed. The overall lower level of the S/N ratio than that predicted by the theory is most likely due to the buildup of background light-scattering recorded along with the holograms.

The measurements and calculations shown in Figs. 7 to 10 were made for the recordings of 50 holograms. The calculations indicated that an increase beyond this number did not decrease the S/N ratio significantly, as long as the angular separation was $\gtrsim$0.1°. This was checked by recording 200 holograms at 0.10° in the 0.826-cm-thick crystal. The measured S/N ratio was 39 dB, as compared with 37 dB for 50 holograms. The difference is within the scatter in the data. An angular spacing in air of $\gtrsim$0.10° is required in order to store $\gtrsim$500 holograms in a $LiNbO_3$ crystal.

Zech [18] has measured crosstalk noise in 0.50- to 2.0-mm-thick samples of different organic storage media. His measurements differ from those reported here in that the total exposure was divided equally among the holograms recorded. Therefore, as the number of holograms increased, the exposure per hologram was $\propto 1/N$, and the diffraction efficiency per hologram was $\propto 1/N^2$. The observed S/N ratio was found to decrease at $1/N^2$, corresponding to a decreasing signal intensity and fixed noise intensity arising from defect scattering. This result is unrelated to the results presented here since we have recorded holograms with equal exposure (when we account for optical and thermal erasure). The noise, in our case, arises primarily from the crosstalk between

holograms. This latter approach is the more relevant one, since it represents the situation which will be used in practice.

In summary, the measurements presented here show that the effect of hologram crosstalk can be estimated using a model based upon incoherent addition of the intensities of the off-Bragg holograms. The S/N ratio is oscillatory with a period inversely proportional to the effective grating thickness for angular spacings $\gtrsim 0.1°$. The measurements also show that high ($\gtrsim 40$ dB) S/N ratio can be obtained with a reasonable $\gtrsim 0.1°$ angular spacing between holograms, but due to the oscillatory nature of the S/N ratio vs angular spacing, the effective grating thickness must be determined. The hologram spacing should be chosen to correspond to a peak in the S/N ratio, which can be calculated from Kogelnik's theory [24].

IV. INTERMODULATION DISTORTION

Nonlinear effects are well known in the field of thin-phase holograms, where they have received considerable attention both in the understanding of the mechanisms involved and the suppression of their influence on the readout image. These nonlinearities are of two types. The first arises from a nonlinearity in the photoinduced change in the material properties (absorption or index of refraction changes), or as is the case with photoresist, a nonlinearity in the etching rate during processing after exposure [16]. The second nonlinearity, commonly known as intermodulation noise (IM), arises from the interference of the object beam with itself, in addition to its interference with the reference beam [16,25]. This interference gives rise to a low spatial frequency modulation of the material properties, which is in addition to the higher spatial frequency modulation due to the interference with the reference beam. This low-frequency modulation causes multiple ghost images of the image which is reconstructed from the hologram by the readout beam. The magnitude of this effect in thin-phase holograms is controlled by recording the hologram with a reference/object beam ratio much greater than one.

In the case of thick-phase holograms, nonlinearities in both the recording medium and the recording process have been considered by several workers [17,18]. They have been concerned primarily with noise sources in photographic emulsions ($\sim$6 μm thick) and in photodegradable plastics ($\sim$500 μm thick). Zech has observed intermodulation distortion in a 500-μm layer of a plastic medium, and observed a suppression of the IM in the Bragg plane [18].

In this section we present measurements of the dependence of the index of refraction on exposure in iron-doped $LiNbO_3$ to determine the degree of linearity. We also present a detailed calculation of intermodulation noise and our measurements of this effect.

A. MATERIAL LINEARITY

The photoinduced refraction index changed in iron-doped $LiNbO_3$ produced by the 488.0-nm Ar^+ laser line was measured with a Mach-Zehnder interferometer. The sample is inserted in one arm of the interferometer, and a portion

25. J. A. Jenney, Appl. Opt. 11, 1371 (1972).

of the sample is irradiated through a mask with the Ar^+ laser beam, as shown in Fig. 14. The fringe pattern may be observed either by viewing at right angles to the Ar^+ irradiating beam, or by rotating the sample after the exposure to view in the same direction as that of the 488.0-nm beam. In the former case, the value of t is the width of the 488.0-nm beam in the direction of the interferometer beam, whereas, in the latter case, the thickness is the length of the sample along the 488.0-nm beam direction. We find that the results obtained by these two methods agree within the accuracy of the measurement of the fringe shift.

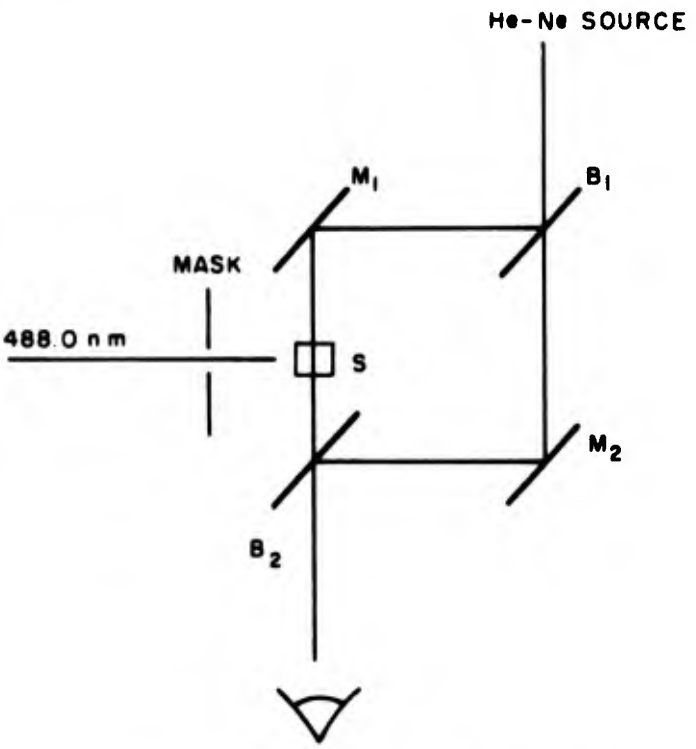

Figure 14. Schematic diagram of a Mach-Zehnder interferometer.

A change in the refractive index in the irradiated region of the sample produces a fringe shift in the interference pattern viewed with the interferometer source. The fringe shift across the boundary between exposed and virgin areas of the sample was recorded photographically, and the refractive index change is obtained from the measured fringe shift by the equation

$$\Delta n = \frac{\delta \lambda_{MZ}}{t} \tag{8}$$

where δ is the fringe shift, λ_{MZ} is the wavelength of the interferometer source (632.8 nm), and t is the thickness of the irradiated region in the direction of the interferometer beam.

The photoinduced refraction index change was measured for a sample before and after reduction. The sample was cut and polished to a flatness of $\lambda/4$ over a 1-cm^2 area and was oriented with the c-axis parallel to the polarization direction of the electric vector of both the 488.0 nm and 632.8 nm beams.

Figures 15(a) and (b) show the fringe pattern at 632.8 nm before exposure to the 488.0-nm Ar^+ laser light and after an exposure of 13.4 J/cm^2. The fringes are reasonably straight, and the width of the fringe was about one tenth of the spacing, which enabled us to measure values of Δn as small as 2×10^{-5}. The results of a series of measurements of Δn as a function of incident exposure are shown in Fig. 16. Data for both before and after reduction are included on the plot, and the data for the sample before reduction were corrected for its lower absorption compared with that after reduction to correspond to the absorption of the reduced sample. The measured absorption constants at 488.0 nm before and after reduction are 0.713 cm^{-1} and 0.997 cm^{-1}, respectively.

From the data shown in Fig. 16, it is clear that Δn depends linearly on incident exposure over the range 0.6 to 6 J/cm^2, using incident intensities between 0.2 and 0.35 W/cm^2. This is well beyond the range used for the recording of holograms in thick crystals of iron-doped $LiNbO_3$. For example, in a 0.5-cm-thick crystal, an index change of $\sim 2 \times 10^{-5}$ is required for a 10% efficient hologram. Based on these results, we consider the change in index of refraction with exposure to light to be linear over the range of interest for our work.

B. INTERMODULATION NOISE

1. Physical Origin of the Intermodulation Noise

The intermodulation noise (IM noise) is a form of hologram noise inherent in the hologram recording process. To explain its physical origin, we consider the model in which the object beam is composed of two plain waves.* It is a

*Such a model has been used by Jenney [25] to calculate the IM noise in thin-phase holograms.

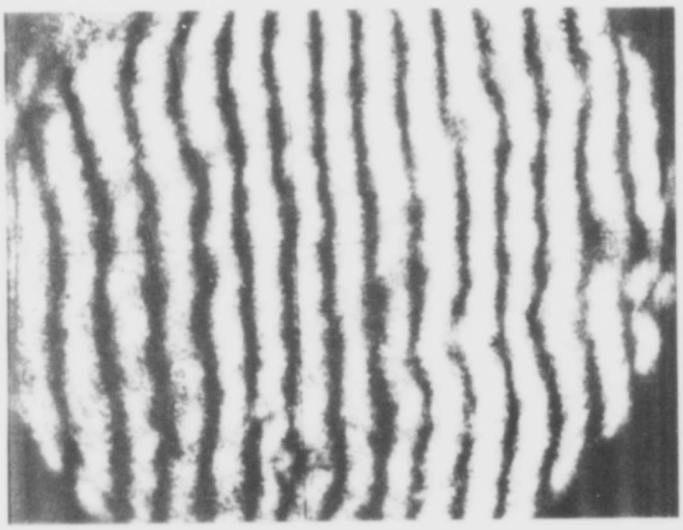

(a)

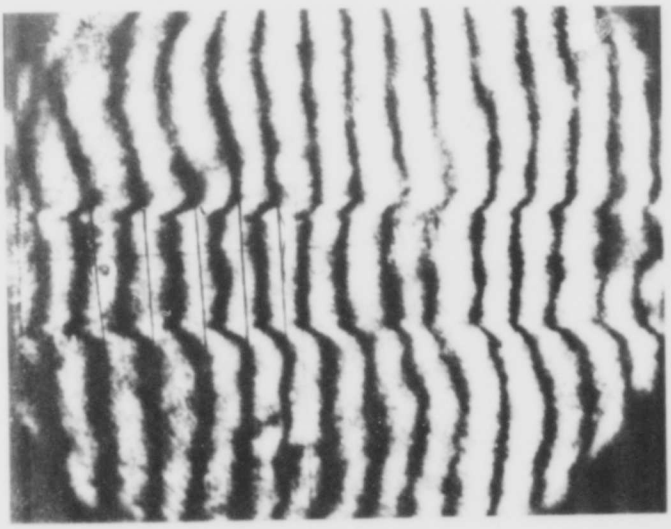

(b)

Figure 15. Mach-Zehnder fringe pattern at 632.8 nm (a) before explosure to the 488.0-nm Ar^+ laser light (b) after an exposure of 13.4 J/cm^2.

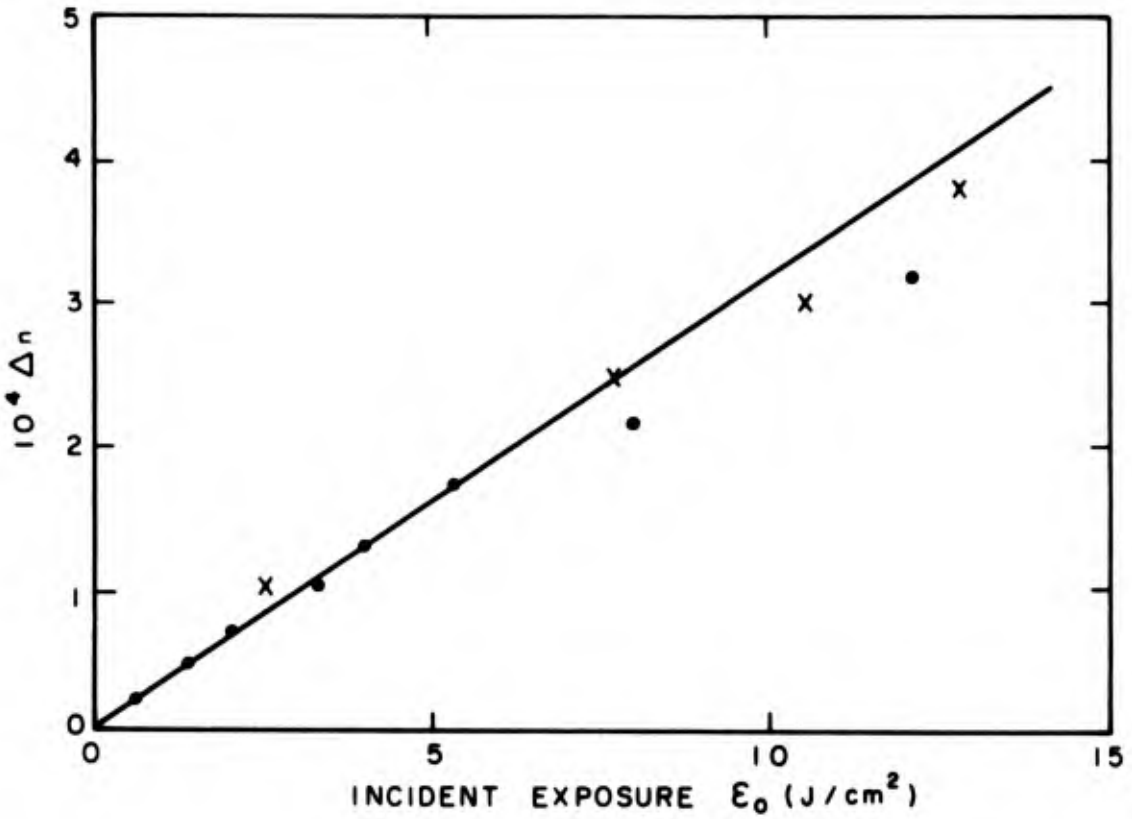

Figure 16. Plot of the measured index of refraction change Δn vs incident exposure at 488.0 nm before and after reduction.

simplification of the realistic case in that we use two plain waves instead of infinitely many plain waves to represent the object beam. As seen below, the model is sufficient to explain the physics of the IM noise and can be used to calculate its magnitude.

In Fig. 17 we show the three-beam recording geometry. The reference beam is dencted by R, and the two object beams are denoted 1 and 2. For simplicity, we take the surrounding medium as having the same index of refraction as the recording crystal so that there will be no refraction of the beams as they enter the crystal. The complex amplitudes of the three beams are taken to be A_R, A_1, and A_2. The amplitudes are related to the intensities I_R, I_1, and I_2 by the relationship

$$A_{R,1,2} = \sqrt{I_{R,1,2}} \exp \left[i\phi_{R,1,2}\right] \tag{9}$$

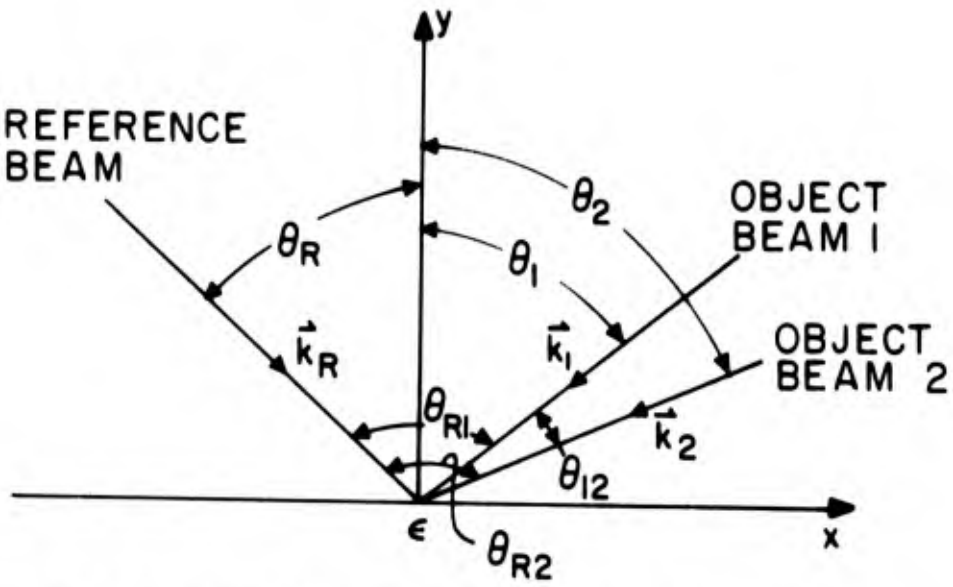

Figure 17. Schematic diagram of the three-beam recording geometry.

where $\phi_{R,1,2}$ is the phase angle of the designated beam. The wave vectors of the three beams are denoted by $\vec{k}_R$, $\vec{k}_1$, and $\vec{k}_2$, with

$$|\vec{k}_R| = |\vec{k}_1| = |\vec{k}_2| \equiv \beta = \sqrt{\varepsilon_o}\ (\omega/c) \tag{10}$$

where $||$ denotes the magnitude of the vector, ε_o is the average dielectric constant of the recording crystal, ω is the angular frequency of light, and c is the speed of light in vacuum. As the three beams enter the crystal, they coherently interfere with each other, giving rise to an intensity pattern which can be calculated as

$$\begin{aligned} I(\vec{r}) &= \left| A_R \exp(i\vec{k}_R\cdot\vec{r}) + A_1 \exp(i\vec{k}_1\cdot\vec{r}) + A_2 \exp(i\vec{k}_2\cdot\vec{r}) \right|^2 \\ &= I_R + I_1 + I_2 + 2\sqrt{I_R I_1}\cos\left[(\vec{k}_R - \vec{k}_1)\cdot\vec{r} + (\phi_R - \phi_1)\right] \\ &\quad + 2\sqrt{I_R I_2}\cos\left[(\vec{k}_R - \vec{k}_2)\cdot\vec{r} + (\phi_R - \phi_2)\right] \\ &\quad + 2\sqrt{I_1 I_2}\cos\left[(\vec{k}_1 - \vec{k}_2)\cdot\vec{r} + (\phi_1 - \phi_2)\right] , \end{aligned} \tag{11}$$

where $\vec{r}$ is the vector which denotes spatial position. The phase factors $(\phi_R - \phi_1)$, $(\phi_R - \phi_2)$ can be eliminated by redefining the origin of the spatial coordinate. That is, if we define $\vec{r}' = \vec{r} + \vec{p}$ where $\vec{p}\cdot(\vec{k}_R - \vec{k}_1) = \phi_R - \phi_1$ and $\vec{p}\cdot(\vec{k}_R - \vec{k}_2) = \phi_R - \phi_2$, Eq. [11] can be rewritten as

$$I(\vec{r}') = I_R + I_1 + I_2 + 2\sqrt{I_R I_1}\cos(\vec{K}_1 \cdot \vec{r}') + 2\sqrt{I_R I_2}\cos(\vec{K}_2 \cdot \vec{r}') + 2\sqrt{I_1 I_2}\cos(\vec{K}_{12} \cdot \vec{r}'), \quad (12)$$

where

$$\vec{K}_1 \equiv \vec{k}_R - \vec{k}_1$$

$$\vec{K}_2 \equiv \vec{k}_R - \vec{k}_2$$

$$\vec{K}_{12} \equiv \vec{k}_1 - \vec{k}_2$$

It should be remarked that usually $|\vec{K}_{12}| << |\vec{K}_1|, |\vec{K}_2|$ since the angle of separation between $\vec{k}_1$ and $\vec{k}_2$ is smaller than that between $\vec{k}_1$ and $\vec{k}_R$ (or that between $\vec{k}_2$ and $\vec{k}_R$). When the intensity pattern given by Eq. (12) is imposed on the recording crystal, the optical dielectric constant at each point will be changed according to the intensity of light at that point. If the recording medium is *linear*, then the magnitude of the dielectric constant deviation from the average is linearly proportional to the intensity. That is,

$$\varepsilon(r) = \varepsilon'_o [1 + \alpha I(\vec{r})] \quad (13)$$

where $\varepsilon(r)$ is the dielectric constant at point r, ε'_o is the dielectric constant of the crystal when there is no light, and α is some material constant relating the intensity of the light to the change in the dielectric constant. Substitution of Eq. (12) into Eq. (13) yields

$$\varepsilon(\vec{r}) = \varepsilon_o + \varepsilon_1 \cos[\vec{K}_1 \cdot \vec{r}] + \varepsilon_2 \cos[\vec{K}_2 \cdot \vec{r}] + \varepsilon_{12} \cos[\vec{K}_{12} \cdot \vec{r}] \quad (14)$$

where

$$\varepsilon_o = \varepsilon_o' [1 + \alpha(I_R + I_1 + I_2)]$$

$$\varepsilon_1 = \varepsilon_o' \alpha \sqrt{I_R I_1}$$

$$\varepsilon_2 \quad \varepsilon_o' \alpha \sqrt{I_R I_2}$$

$$\varepsilon_{12} = \varepsilon_o' \alpha \sqrt{I_1 I_2}$$

and we have omitted the prime on $\vec{r}$. It should be noted that usually ε_1, ε_2, $\varepsilon_{12} << \varepsilon_o$. Therefore, we can write the index of refraction $n(\vec{r})$ as

$$n(\vec{r}) = \sqrt{\varepsilon(\vec{r})} \simeq n_o + n_1 \cos[\vec{K}_1 \cdot \vec{r}] + n_2 \cos[\vec{K}_2 \cdot \vec{r}] + n_{12} \cos[\vec{K}_{12} \cdot \vec{r}], \qquad (15)$$

where $n_{1,2,12} \equiv \varepsilon_{1,2,12} / 2\sqrt{\varepsilon_o}$, $n_o \equiv \sqrt{\varepsilon_o}$.

We are now in the position to see the origin of the IM noise. When a reconstruction beam (R) having the same wave vector as the reference beam is incident on a crystal with the dielectric constant modulation of Eq. (14), it will be diffracted by the various gratings into various signal and noise beams. This is apparent from the Bragg diagram shown in Fig. 18. First of all, diffraction by grating $\vec{K}_1$ and $\vec{K}_2$ will give rise to signal beams S_1 and S_2 and conjugate signal beams S_1^* and S_2^*. However, since S_1^* and S_2^* do not satisfy the Bragg condition (as is apparent from the Bragg diagram), their magnitudes will be much smaller than S_1 and S_2. Next, let us consider the effect of the grating $\vec{K}_{12}$. $\vec{K}_{12}$ would diffract R into two noise beams M and M^*. Also, it would diffract S_1 and S_2 into each other and into two noise beams N_1 and N_2. N_1 and N_2 are called the intermodulation noise. Since $|\vec{K}_{12}|$ is usually much smaller in magnitude than $|\vec{K}_1|$ or $|\vec{K}_2|$, N_1 and N_2 are only slightly off the Bragg condition and therefore should be larger in magnitude than S_1^* AND S_2^*. Also, since $|\vec{K}_{12}|$ is small, N_1 and N_2 are close to S_1 and S_2 in terms of angular separation and therefore cannot easily be eliminated, as in the case of M and M^*, by limiting the readout angle.

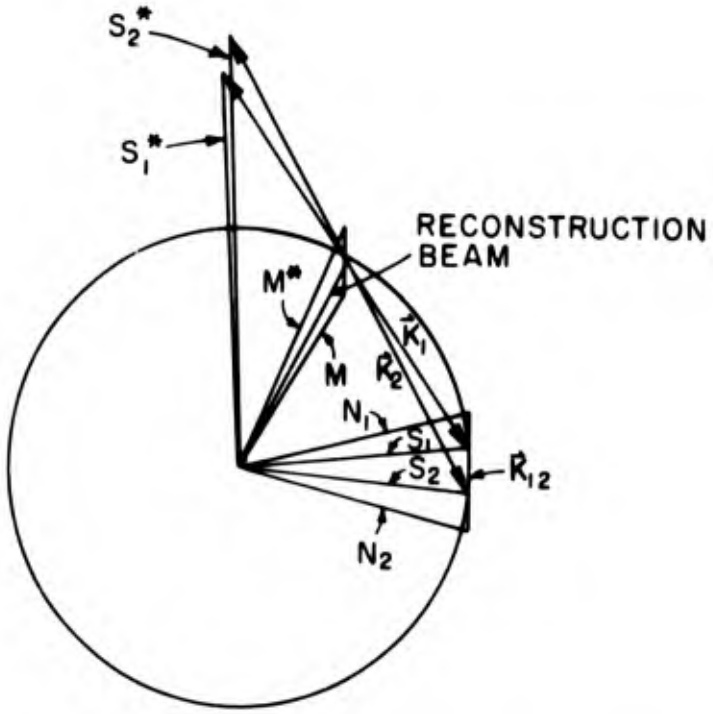

Figure 18. Bragg diagram relating the readout beam to the signal and noise beams and the grating vectors.

From the above discussion it is clear that the grating $\vec{K}_{12}$, which is formed during recording by the coherent interference of the two object beams 1 and 2, is the cause for IM noise. In the following calculation it will be shown that the magnitude of IM noise is a sensitive function of the crystal thickness. For thick volume phase holograms the IM noise is negligible. However, for thin holograms, the problem of IM noise is a well-known experimental fact. It is proposed, that for thin holograms, the elimination of $\vec{K}_{12}$ is an effective method to greatly reduce the IM noise. This can be achieved if the recording is done in such a way that beam 2 is blocked while beam 1 is recorded, and then beam 1 is blocked while beam 2 is recorded. In realistic cases, this means the introduction of a pinhole (not too small to cause diffraction) between the object lens and the sample. The pinhole can be moved slowly across the whole object beam so that at any particular time only a particular angular component of the object beam is being recorded. This method should be equally applicable to IM noise arising from recording nonlinearities.

2. Coupled-Wave Theory Calculation

In this section we calculate the magnitude of the IM noise by using the coupled-wave theory [24]. The object of the coupled-wave theory is the solution of the scalar wave equation:

$$\nabla^2 E(\vec{r}) + \frac{\omega^2}{c^2} \varepsilon(\vec{r})\, E(\vec{r}) = 0 \tag{16}$$

where $E(\vec{r})$ is the magnitude of the electric field vector at point $\vec{r}$. In our present case $E(\vec{r})$ is given by

$$\begin{aligned} E(\vec{r}) = {} & R(y) \exp[-i\vec{k}_o\cdot\vec{r}] + S_1(y) \exp[-i(\vec{k}_o - \vec{K}_1)\cdot r] \\ & + S_2(y) \exp[-i(\vec{k}_o - \vec{K}_2)\cdot\vec{r}] + N_1(y) \exp[-i(\vec{k}_o - \vec{K}_{12})\cdot r] \\ & + N_2(y) \exp[-i(\vec{k}_o - \vec{K}_2 - \vec{K}_{12})\cdot\vec{r}]. \end{aligned} \tag{17}$$

Here y is the direction perpendicular to the crystal thickness, $\vec{k}_o$ is the wave vector of the readout beam, and R_1, S_1, S_2, N_1, N_2 are the amplitudes of the readout, signal 1, signal 2, and IM noise beams, respectively. In Eq. (17) we have neglected conjugate signal terms, M, M^*, and all other higher order terms. Substituting Eqs. (17) and (14) into Eq. (15), collecting terms with the same exponentials, and neglecting terms like R"(y), S_1"(y), S_2"(y), N_1"(y), N_2"(y) (" means second derivative with respect to y), we get

$$C_o R'(y) = -iK_1 S_1(y) - iK_2 S_2(y) \tag{18(a)}$$

$$C_{S1} S_1'(y) + i\vartheta_1 S_1(y) = -iK_1 R(y) - iK_{12} S_2(y) - iK_{12} N_1(y) \tag{18(b)}$$

$$C_{S2} S_2'(y) + i\vartheta_2 S_2(y) = -iK_2 R(y) - iK_{12} S_1(y) - iK_{12} N_2(y) \tag{18(c)}$$

$$C_{N1} N_1'(y) - i(\Delta - 2\vartheta_1 + \vartheta_2) N_1(y) = -iK_{12} S_1(y) \tag{18(d)}$$

$$C_{N2} N_2'(y) - i(\Delta - 2\vartheta_2 + \vartheta_1) N_2(y) = -iK_{12} S_2(y). \tag{18(e)}$$

Here C_o, C_{S1}, C_{S2}, C_{N1}, C_{N2} are the directional cosines of the various beams. For example, $C_o = (\vec{k}_o)_y/\beta$ and $C_{S1} = (\vec{k}_o - \vec{K}_1)_y/\beta$, where $(\ )_y$ means the magnitude of the y-component. The other quantities which appear in Eqs. (18a) - (18e) are defined as follows:

$$K_{1,2,12} \equiv \beta\varepsilon_{1,2,12}/4\varepsilon_o = \pi n_{1,2,12}/\lambda \tag{19}$$

where λ is the wavelength of light in air,

$$\vartheta_{1(2)} \equiv \beta\,|\sin\theta_{R1(R2)}|\Delta\theta \tag{20}$$

where $||$ means absolute value, $\theta_{R1(R2)}$ is the angle as shown in Fig. 17 for the recording geometry, and $\Delta\theta$ is the angle of deviation of $\vec{k}_o$ from the direction of $\vec{k}_R$. The sign of $\Delta\theta$ is such that $\Delta\theta > o$ implies $|\vec{k}_o - \vec{K}_1| < \beta$.

$$\Delta \equiv 2\beta(1 - \cos\theta_{12}), \tag{21}$$

where θ_{12} is the angle between the two object beams as shown in Fig. 17.

The neglect of second-order derivatives in Eqs. (18a) to (18e) is justified on the basis that R, S_1, S_2, N_1, and N_2 are slowly varying functions of y, which is usually the case. Equations (18a) to (18c) are the coupled wave equations for the quantities R, S_1, S_2, N_1, and N_2. The boundary conditions for these quantities are:

$$R(o) = 1,\ S_1(o) = S_2(o) = N_1(o) = N_2(o) = 0. \tag{22}$$

The rigorous solution of Eqs. (18a) - (18e) with the conditions given by Eq. (22) is difficult. We will make some simplifying approximations which will facilitate the mathematics involved. First, we will drop the term $-iK_{12}N_1(y)$ from Eq. (18b) and the term $-iK_{12}N_2(y)$ from Eq. (18c), since N_1, N_2 are expected to be small compared with S_1 and S_2. Second, we will drop $-iK_{12}S_2(y)$ from Eq. (18b) and the term $-iK_{12}N_2(y)$ from Eq. (18c), since these terms only have the effect of coupling S_1 and S_2 and tending to equalize the amplitude of S_1 and S_2. Therefore, if we are dealing with the case of $K_1 \simeq K_2$ (and, therefore, $S_1 \simeq S_2$), such an approximation should have negligible effect on the

solution. Third, we will set $\vartheta_1 = \vartheta_2 = \vartheta$ and $C_{S1} = C_{S2} = C_{N1} = C_{N2} = C_S$. This approximation is based on the observation that since θ_{12} is usually small, $\theta_{R1} \simeq \theta_{R2}$, and the direction cosines C_{N1} and C_{N2} are not very different from C_{S1} and C_{S2}. ϑ and C_S are defined as

$$\vartheta \equiv \beta \, |\sin \theta_{RS}| \Delta\theta \ , \tag{23a}$$

$$C_S = \cos \theta_S \ , \tag{23b}$$

where $\theta_{RS} \equiv (\theta_{R1} + \theta_{R2})/2$, and $\theta_S \equiv (\theta_1 + \theta_2)/2$. θ_{R1}, θ_{R2} θ_1, and θ_2 are defined in Fig. 17. It should be noted that we have approximated C_{S1} and C_{S2}, which are the direction cosines of the signal beams, by $\cos \theta_S$, where θ_S is given in terms of the recording angles. Such an approximation is valid, provided $\Delta\theta$ is small.

With the above approximations, Eqs. (18a) - (18e) become

$$C_o R'(y) = -iK_1 S_1(y) - iK_2 S_2(y) \tag{24a}$$

$$C_S S_1'(y) + i\vartheta S_1(y) = -iK_1 R(y) \tag{24b}$$

$$C_S S_2'(y) + i\vartheta S_2(y) = -iK_2 R(y) \tag{24c}$$

$$C_S N_1'(y) - i(\Delta - \vartheta) N_1(y) = -iK_{12} S_1(y) \tag{24d}$$

$$C_S N_2'(y) - i(\Delta - \vartheta) N_2(y) = -iK_{12} S_2(y). \tag{24e}$$

The solution of Eqs. (24c) - (24e) can be divided into two steps. Equations (24a) - (24c) can be solved first for R, S_1, and S_2. S_1 and S_2 can then be substituted in Eqs. (24d) and (24e) to get N_1 and N_2. Details of the mathematics are presented in the Appendix. It suffices to say here that the solution yields the amplitudes N_1 and N_2 as they emerge from a crystal of thickness d. The diffraction efficiency for the noise is then defined as

$$\eta_{N_{1,2}} = \frac{C_S}{C_o} N^*_{1,2}(d) \, N_{1,2}(d) \ . \tag{25}$$

For the case of $K_1 = K_2$, we have $S_1 = S_2 = S$ and $N_1 = N_2 = N$. Substituting the solution for N(d) into Eq. (25) yields

$$\eta_N = \frac{1}{C_o C_S^3} \frac{K_1^2 K_{12}^2}{\Gamma^4} \frac{1}{\left[\frac{\Lambda^2}{\Gamma^2} - 1\right]} \left\{ \left[2 - (1 - \frac{\Lambda^2}{\Gamma^2}) \sin^2 \Gamma d - (1 + \frac{\Lambda}{\Gamma}) \cos(\Lambda - \Gamma) d \right.\right.$$

$$\left.\left. - (1 - \frac{\Lambda}{\Gamma}) \cos(\Lambda + \Gamma) d \right] \frac{1}{\left[\frac{\Lambda^2}{\Gamma^2} - 1\right]} \right\} , \tag{26}$$

where

$$\Gamma \equiv \frac{\pi n_o}{\lambda C_S} \sqrt{\sin^2 \theta_{RS} \, (\Delta\theta)^2 + \frac{C_S}{C_o} \frac{2n_1^2}{n_o^2}} \quad , \tag{27}$$

$$\Lambda \equiv \frac{\pi n_o}{\lambda C_S} \left[4(1 - \cos \theta_{12}) - |\sin \theta_{RS}| \Delta\theta \right] \quad . \tag{28}$$

Similarly, the diffraction efficiency for the signal S is given by

$$\eta_s = \frac{1}{C_o C_S} \frac{K_1^2}{\Gamma^2} \sin^2 \Gamma d \quad . \tag{29}$$

3. Discussion of the Calculation

The diffraction efficiency for the IM noise given by Eq. (26) consists of two parts. One is the trigonometric function (in curly bracket) which determines the oscillation of the function. This part of the function has the order of magnitude of 1. It is seen here that as a function of $\Delta\theta$, the oscillation period of η_N is a decreasing function of d. The other part is the envelope function, which determines the order of magnitude of η_N. Since we are interested in the S/N ratio, it is appropriate to compare the envelope functions for η_N and η_S. From Eqs. (26) and (29) it is clear that

$$O(\eta_N/\eta_S) \simeq \frac{1}{C_S^2} \frac{K_{12}^2}{\Gamma^2} \frac{1}{\left[\frac{\Lambda^2}{\Gamma^2} - 1\right]} , \tag{30}$$

where the symbol O denotes the order of magnitude of the quantity inside the bracket. Writing out all the pertinent factors explicitly, we get

$$O(\eta_N/\eta_S) \simeq \frac{I_1}{I_R} \left\{ \frac{n_1^2}{n_o^2} \frac{1}{\left(\sin^2\theta_{RS}(\Delta\theta)^2 + \frac{C_S}{C_o}\frac{2n_1^2}{n_o^2} \right)} \right\}$$

$$\frac{1}{\left[\frac{(4(1-\cos\theta_{12}) - |\sin\theta_{RS}|\Delta\theta)^2}{\left(\sin^2\theta_{RS}(\Delta\theta)^2 + \frac{C_S}{C_o}\frac{2n_1^2}{n_o^2} \right)} - 1 \right]} \qquad (31)$$

It is apparent from Eq. (31) that the magnitude of η_N/η_S is governed by three factors. The first is (I_1/I_R), the ratio of object beam intensity to reference beam intensity. This factor is well-known in the problem of IM noise in thin holograms. The next two factors deserve more analysis. For simplicity, let us label the factors in curly brackets ({}) as P and the last factor in Eq. (31) as Q. As a function of $\Delta\theta$, we see that at $\Delta\theta = 0$ the value of P is the order of unity, but that

$$Q = \frac{C_S n_1^2/C_o n_o^2}{\left[2(1-\cos\theta_{12}) - \frac{C_S n_1^2}{C_o n_o^2} \right]} \qquad (32)$$

is usually very small for volume phase holograms. The reason for this smallness is twofold. First, we have a non-zero factor $2(1 - \cos\theta_{12})$ which arises from the fact that the IM noise beams do not satisfy the Bragg condition. As we see from Eq. (32), a non-zero $(1 - \cos\theta_{12})$ is essential to guarantee that $Q \neq 1$. Second, given a non-zero $(1 - \cos\theta_{12})$, the smallness of Q rests on the fact that in a volume phase hologram $(n_1/n_o) \simeq 10^{-5} - 10^{-4}$. Therefore, we can extract one piece of physics from the solution, Eq. (26). That is, at $\Delta\theta = 0$, the attenuation of the IM noise in the volume phase holograms results from the fact that for a *given signal diffraction efficiency* the index of refraction

modulation n_1 is smaller for the thick than for the thin holograms. In fact, n_1 is inversely proportional to d. Therefore, thick holograms have a distinct advantage over the thin holograms in regard to IM noise with a factor of $(1/d)^2$.

As $\Delta\theta$ (in radians) deviates from zero and becomes larger than n_1 in magnitude, the factor P becomes small ($P \sim n_1^2$), and the factor Q is of the order of the ratio $(\Delta\theta)^2 / [4(1 - \cos\theta_{12})]^2$. An interesting phenomenon happens when $\Delta\theta$ is positive and large, there is a value of $\Delta\theta$ at which $Q \to \infty$, which is apparent from Eqs. (18) and (19). This will happen at approximately

$$\Delta\theta \simeq \frac{2(1 - \cos\theta_{12})}{|\sin\theta_{RS}|} \quad . \tag{33}$$

At first glance, this divergence may seem to imply that $\eta_N \to \infty$, which is an unphysical result. However, a closer examination of Eq. (26) reveals that the trigonometric part vanishes at exactly the same point. The net result is that η_N at that point has the value

$$\eta_N = \frac{1}{C_o C_S^3} \frac{K_1^2 K_{12}^2}{4\Gamma^4} \left\{ \Gamma^2 d^2 + \sin^2 \Gamma d - 2\Gamma d \sin \Gamma d \cos \Gamma d \right\} \tag{34}$$

It may seem that η_N given by Eq. (34) can be arbitrarily large for $d \to \infty$. This is the artifact of the approximation made earlier in dropping N_1 and N_2 from Eqs. (18b) and (18c). Therefore, Eq. (34) is only valid when η_N is small compared with η_S. However, the point to be made here is that η_N will have a maximum at a value of $\Delta\theta$, approximately given by Eq. (33). The physical origin of this peak lies in the fact that at the value of $\Delta\theta$ given by Eq. (33), the IM noise beam satisfies the Bragg condition, which is given by

$$|\vec{k}_o - \vec{K}_1 + \vec{K}_{12}| = \beta \tag{35}$$

It is a simple exercise to show that the condition given by Eq. (35) directly implies the relation of Eq. (33), provided that θ_{12} is small. If θ_{12} is not small, then Eq. (33) is modified to read

$$\Delta\theta = \frac{2(1 - \cos\theta_{12})}{[2|\sin\theta_{R2}| - |\sin\theta_{R1}|]} \tag{33a}$$

In Fig. 19 we show the results of numerical calculations. The features we discussed above are clearly demonstrated in the plot. In particular, we note that an increase of crystal thickness by a factor of ten lowers the IM noise level by 40 dB and that the peak of IM noise occurs at the value of $\Delta\theta$ given by Eq. (28).

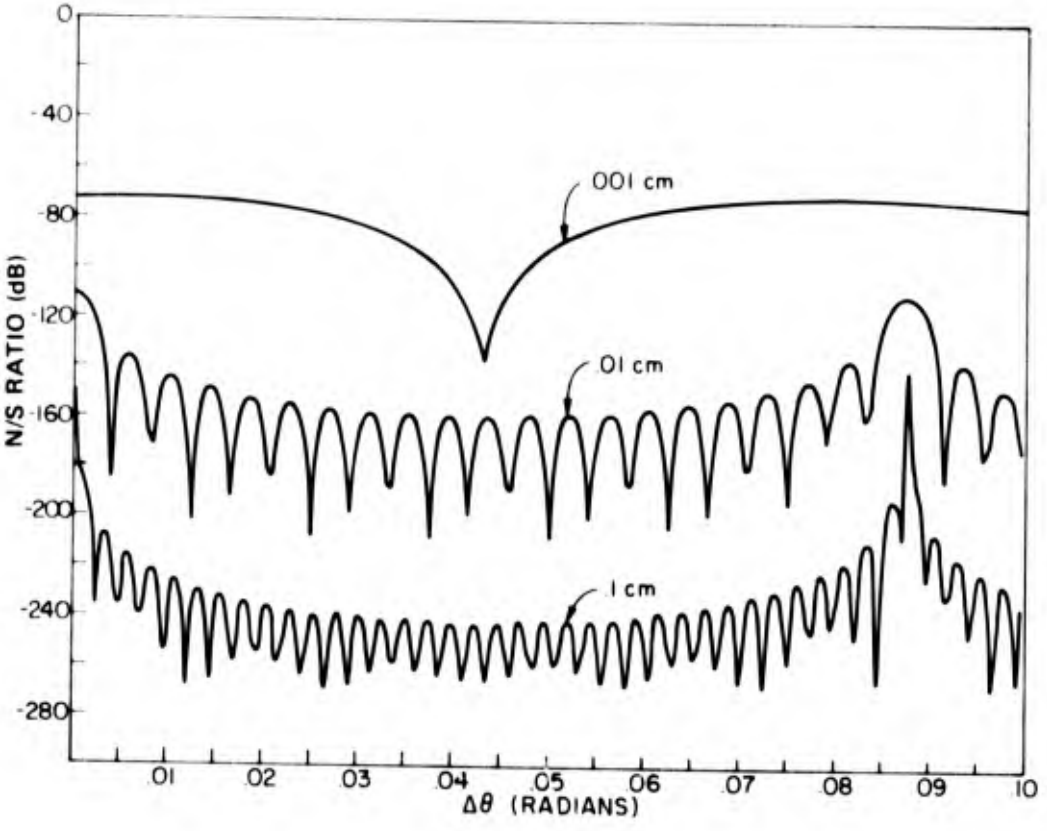

Figure 19. Theoretical N/S ratio due to intermodulation distortion as a function of the angular deviation in the crystal from the Bragg condition for a beam ratio of 1 and $\theta_{12} = 12°$.

Before leaving this section we would like to make some remarks on the coupling effect of the grating $\vec{K}_{12}$ on the two signal beams. As mentioned earlier, in deriving Eq. (26) we have neglected the coupling effect of $\vec{K}_{12}$ by dropping the terms $-iK_{12}S_1$ and $-iK_{12}S_2$ from Eqs. (18b) and (18c). The rationale given there is that these terms would not affect the two signal beam intensities as long as S_1 is comparable to S_2. What happens when $S_1 >> S_2$, or vice versa? We believe the effect of $\vec{K}_{12}$ in that case would be to increase the intensity of the weaker signal beam at the expense of the

stronger one. As an example, let us consider a target object which consists of a high-frequency and a low-frequency component, with the two components having a high contrast ratio. When the recording beam passes through the object, it is split into two beams, one carrying the information of the high-frequency component and the other beam carrying the information of the low-frequency component. These two beams are identified as object beams 1 and 2 in our model. Therefore, the effect of $\vec{K}_{12}$ here is to reduce the contrast ratio of the two components in the reconstructed image. Such an effect, which can be called intensity leveling, is yet to be observed and can be a subject of further study.

C. EXPERIMENTAL RESULTS

1. Measurements

To confirm the calculation of the magnitude of the IM noise, the two-object beam IM was measured. Two approaches were used in this measurement. The first approach was to rotate the crystal off the Bragg condition for the hologram and measure IM at the appropriate angle. The apparatus used in this approach is shown schematically in Fig. 20. The two object beams are ∿18° apart in angle and their bisector is 30° from the reference beam. The readout light beam is chopped at 50 Hz. The readout image beam, which is therefore

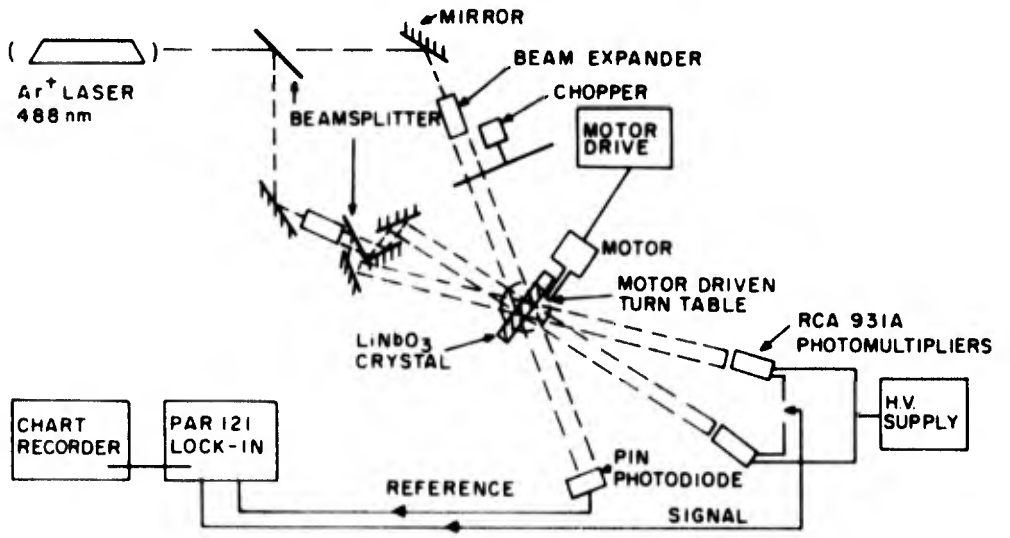

Figure 20. Schematic diagram of the apparatus used to measure intermodulation distortion.

also chopped, is synchronously detected using the PAR-121 lock-in amplifier and displayed on the chart recorded. This technique discriminates against all scattered light except that scattered by the crystal itself. The fraction of the readout beam scattered by the crystal into the image beam channel was $\sim 10^{-5}$. While this scattered light is considered as noise in the image it is essentially constant in time and therefore can be partially offset electronically in the lock-in amplifiers to increase the signal/background noise ratio. Since the readout light scattered from the crystal has an angular dependence [19], the upper of the two detectors shown in Fig. 20 will have the smaller scattered light. It was in the vicinity of that detector that our measurements were made.

To measure the IM noise using this arrangement, a 20% diffraction efficiency hologram was recorded in a 0.2-cm-thick crystal of 0.02 mole % iron-doped $LiNbO_3$ with a beam ratio of 2. The angle of incidence of the reference beam on the crystal was 15° in air to the face normal. The readout beam angle to the grating was varied by rotating the crystal. The chart recording of the detected IM signal is shown in Fig. 21. The IM signal is -143 dB from the on-Bragg signal. The deviation from the Bragg angle in air was 7°. From Eq. (34) and Fig. 19 the calculated amplitude is -156 dB. From Eq. (33), and taking into consideration the refraction of the beams as they enter the crystal, we calculate the deviation in air of the Bragg angle for this angular spacing of the object beams to be 5.8°.

A second approach to the measurement of the IM noise is to measure the on-Bragg IM signal. The on-Bragg signal we measure corresponds to the beam labeled N_2 in Fig. 18. In Fig. 19 this is the peak at $\Delta\theta = 0$, whereas in the first approach we measured the peak which appears at $\Delta\theta = 0.0875$ radian in the case where the angular spacing of the object beams was 12°. In this approach the readout beam remains fixed at the Bragg angle, and the far-field intensity distribution of the readout image is scanned using the scanning photomultiplier. In this case, a 1% hologram was recorded in a 0.0475-cm-thick crystal using a beam ratio of one. The IM signal was observed at $\sim$16.9° in air from the image signal and was -120 dB from the image signal. From Eq. (34) and Fig. 19 we calculate that the IM signal should be -155 dB, and the angular deviation is 16.4°.

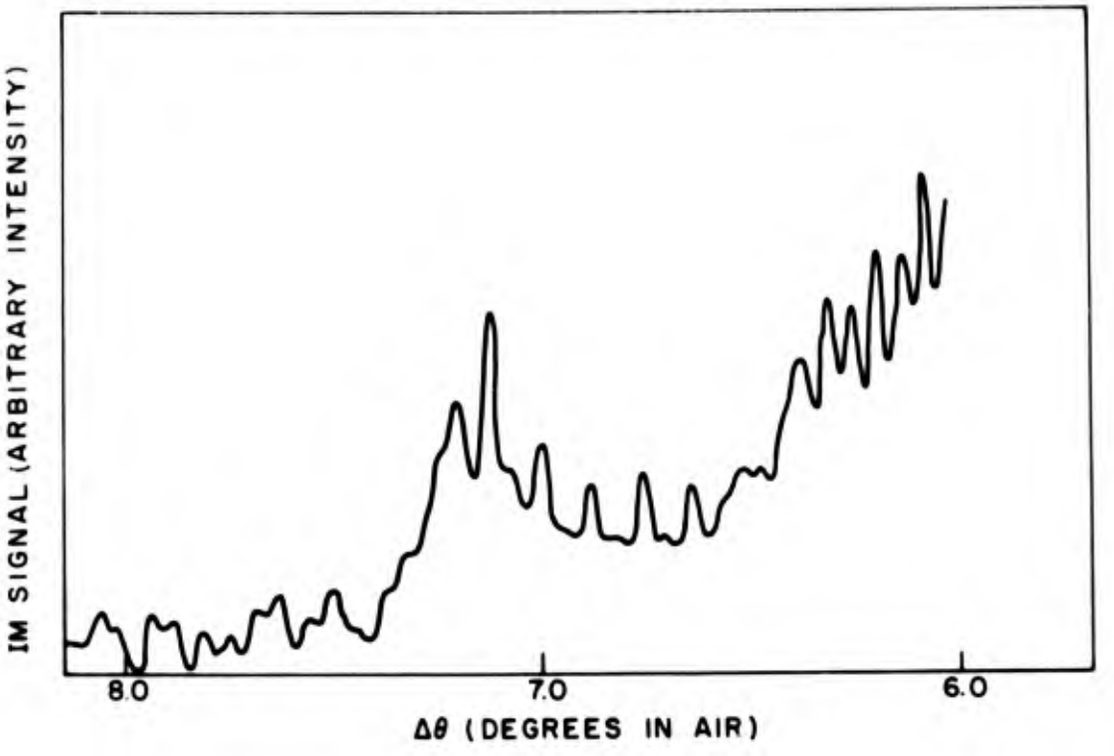

Figure 21. Chart recording of detected IM signal.

Because of the agreement between the observed and calculated angular location of the IM signal we believe that the peaks observed above are, in fact, the IM signal. The magnitude of the observed IM signal is ∿13 dB larger in the first case and ∿35 dB larger in the second case. We do not at present fully understand the reason for this discrepancy between the observed and calculated signal levels. But it should also be noted that due to the neglect of M and M^* (see Eq. (17)) the calculated magnitude of the IM signal is necessarily a lower bound estimate since we have neglected the possibility of the readout beam being scattered into M and M_1^* which, in turn, can be scattered into N_1 and N_2 via $\tilde{K}_1$ and $\tilde{K}_2$. Jenney [25] has also observed an IM signal in thin-phase holograms which ranged up to 10 dB larger than the calculated value.

2. Discussion

There are two sources of nonlinearity which can introduce intermodulation distortion: material nonlinearities and recording nonlinearities due to the coupling of the object beam with itself. Measurements described above show

that iron-doped $LiNbO_3$ is linear over the range of index of refraction modulations typically used. Calculation for the two object beam case show that coupling of the object beam with itself is strongly suppressed. The on-Bragg component is suppressed because the index change is small due to the grating thickness. The off-Bragg component is suppressed by the Bragg condition itself. This was confirmed by measuring both the on- and off-Bragg intermodulation signals.

A typical use of iron-doped $LiNbO_3$ as a volume phase holographic storage media would include recording and fixing 1000 holograms each of 20% diffraction efficiency at a beam ratio of one. The intermodulation signal which appears will be the sum of the on-Bragg term and the off-Bragg contributions of all other holograms. The off-Bragg contributions from other holograms will produce a broad smear-out background because of the continuous range of angles of the light rays which make the object beam. This can be approximated by the two-beam case, as was done above, which produces a single peak. From Fig. 19, we see that each of these IM signals will produce an object signal-to-IM noise ratio of approximately 140 dB. If we allow an additional 30 to 40 dB increase in noise to account for the discrepancy between theory and experiment found above, we are left with a signal-to-IM noise ratio due to IM noise of greater than 90 dB. This is far in excess of the contribution arising from crosstalk and from cosmetic defects in the recording system. We can then conclude that in a typical application IM noise will not make any measurable contribution to the noise.

V. STATISTICAL NOISE

In the preceding sections, it has been assumed that if the recording medium is linear, the pattern of index of refraction modulation is an exact replica of the recording light intensity pattern inside the medium. This assumption will now be examined in more detail.

It is well known that the modulation of the index of refraction in $LiNbO_3$ is achieved by the transport of charges from regions of high recording light intensity to regions of low recording light intensity, the amount of charges transported being proportional to the exposure (intensity of the light x time). Therefore, after the exposure to the recording beams, a charge density pattern will reside in the crystal. The spatial variation of this charge density should be the image of the intensity variation of the recording light in the crystal. However, since charges are point particles, it follows that the charge density pattern is inherently granular in nature, and, as such, can only be an approximation to the continuously varying light intensity pattern. Therefore, the assumption about index of refraction modulation being able to *exactly* reproduce the light intensity pattern cannot be valid, although for high diffraction efficiency holograms (and, therefore, a large number of transported charges) such an assumption is an excellent approximation to the truth.

A. THEORY

From the above, it is clear that when the reconstruction beam enters the crystal, it sees an index of refraction modulation pattern which, due to its granularity, can locally deviate from the recording light intensity pattern. Such deviations would cause additional light scatterings not accounted for by the calculations above. The light scattered by this kind of deviation is called *statistical noise*.

To estimate the magnitude of the statistical noise, we adopt the model of Ramberg [15], in which the statistical noise is treated as an optical analogue of the Debye-Waller effect in x-ray diffraction. As we may recall, the Debye-Waller effect in x-ray diffraction arises from the fact that atoms (or molecules) in a crystal are in constant thermal motion about their equilibrium

positions and, therefore, the x-rays do not see a perfect lattice at any given instant of time. The effect of this random thermal motion by the atoms, according to the work of Debye, is that the x-ray diffraction is insensitive to the exact pattern of deviations of the atoms from their equilibrium positions as long as such deviations are random. However, the intensity of the diffracted x-ray signal is a function of the mean square displacement of the atoms from their equilibrium positions. To be more specific,

$$I = I_o \exp[- \langle u^2 \rangle G^2] \tag{36}$$

where I is the scattered x-ray intensity, I_o is the intensity of light scattered from the rigid lattice (without thermal motions), u is the amplitude of deviation from the equilibrium position, $\langle\ \rangle$ denotes thermal averaging, and G is the magnitude of the grating vector responsible for the diffraction. Equation (36) is well verified experimentally [26].

To apply the Debye theory to the problem of statistical noise in volume phase holograms, we note that instead of atoms, the diffraction grating in our present case is composed of charge density variations. For the purpose of clarity, let us consider the recorded grating of two interfering plain waves. In the ideal case of charge density pattern being the exact image of recording light intensity pattern, the charge density should follow a perfect sinusoidal spatial variation with peaks occurring at $\chi = 0$, d, ---- nd, etc. The ideal peak positions in this case can be compared with the equilibrium positions of the atoms in the x-ray diffraction problem. In the realistic case, the granularity of the charge density pattern would cause deviations from the perfect sinusoidal variation. In particular, if we consider the charges in the region $-(d/4) < \chi < (d/4)$, the center of mass of the charges, χ_c, can deviate from $\chi_c = 0$, the "equilibrium" position. Following the analogy with the Debye-Waller effect in x-ray diffraction, we will attribute the dominant cause of statistical noise to the deviation of χ_c from its "ideal" position. In order to calculate the mean square deviation, we note that the recording light intensity has a sinusoidal variation near $\chi = 0$. Since the probability $P(\chi)$ of trapping a charge at χ is a linear function of the exposure, it

26. C. Kittel, *Introduction to Solid State Physics*, (John Wiley and Sons, Inc., New York, 1971), p. 84.

follows that the form of $P(\chi)$ which peaks at $\chi = 0$ is given by

$$P(\chi) = \frac{\pi}{d} \cos\left(\frac{2\pi\chi}{d}\right), \quad -\frac{d}{4} < \chi < \frac{d}{4} \tag{37}$$

Given the $P(\chi)$ of Eq. (37), it is easily verified that the average value of the center of mass, $\bar{\chi}_c$, is at $\bar{\chi}_c = 0$ (where the overhead bar indicates averaging). However, χ_c can deviate from $\bar{\chi}_c$. The magnitude of the deviation is measured by the quantity

$$\overline{(\chi_c - \bar{\chi}_c)^2} = \overline{\chi_c^2}$$

$\overline{\chi_c^2}$ is analogous to $\langle u^2 \rangle$ in Eq. (36). In order to calculate $\overline{\chi_c^2}$, we note that if there are n electrons in a volume of $(d/2)^3$, then χ_c is defined as

$$\chi_c = \frac{1}{n} \sum_{i=n}^{n} \chi_i$$

Therefore, we can calculate $\overline{\chi_c^2}$ as

$$\overline{\chi_c^2} = \overline{\left[\frac{1}{n} \sum_{i=1}^{n} \chi_i\right]^2} = \frac{1}{n^2} \overline{\left[\sum_{i=1}^{n} \chi_i\right]^2}$$

$$= \frac{1}{n^2} \overline{\left(\chi_1^2 + \chi_2^2 + \ldots + \chi_n^2 + 2\chi_1\chi_2 + 2\chi_2\chi_3 + \ldots\right)}$$

$$= \frac{1}{n^2} \left(\overline{\chi_1^2} + \overline{\chi_2^2} + \ldots + \overline{\chi_n^2}\right)$$

$$= \frac{1}{n} \int_{-d/4}^{d/4} \chi_1^2 P(\chi_1)\, d\chi_1$$

$$= \frac{(\pi^2 - 8)}{16\,\pi^2\, n} d^2 \tag{38}$$

In the above calculation we have assumed that the trapping of every electron is independent of all the others and, therefore, $\overline{\chi_i \chi_j} = 0$ for $i \neq j$. Substituting $\overline{\chi_c^2}$ for $\langle u^2 \rangle$ in Eq. (36) and using the fact that $G = 2\pi/d$, we get

$$I = I_o \exp[-2(\pi^2-8)/Nd^3] \tag{39}$$

where I_o is the intensity of light scattered from a perfect sinusoidal charge density variation, and N is the number of transported charges per cm^3. We note that

$$I_o = I_R \eta_o \tag{40}$$

where I_R is the reconstruction beam intensity and η_o is the diffraction efficiency by a perfect sinusoidal grating as calculated by Kogelnik [23]. Therefore, we can rewrite Eq. (39) as

$$\frac{I}{I_R} \equiv \eta_M = \eta_o \exp[-2(\pi^2-8)/Nd^3] \tag{41}$$

where η_M is defined as the measured diffraction efficiency. Equation (41) tells us that the deviation of measured diffraction efficiency, η_M, from η_o is a function of the number of transported charges. When N is large η_M is almost identical to η_o. However, when N is small, η_M can deviate from η_o significantly. In the experiments discussed below, for a 10% efficient hologram, the amplitude of the index of refraction modulation n_1 is $\sim 1.1 \times 10^{-5}$. For a 0.826-cm-thick crystal, and $d = 0.94$ μm, N is then

$$N = 6.0 \times 10^{19}\, n_1 = 6.6 \times 10^{14}\ cm^{-3}$$

Substituting the values of N and I into Eq. (41), we get

$$\eta_M = \eta_o \exp[-2 \cdot (1.86)/553]$$

$$\simeq 0.9933\, \eta_o \tag{42}$$

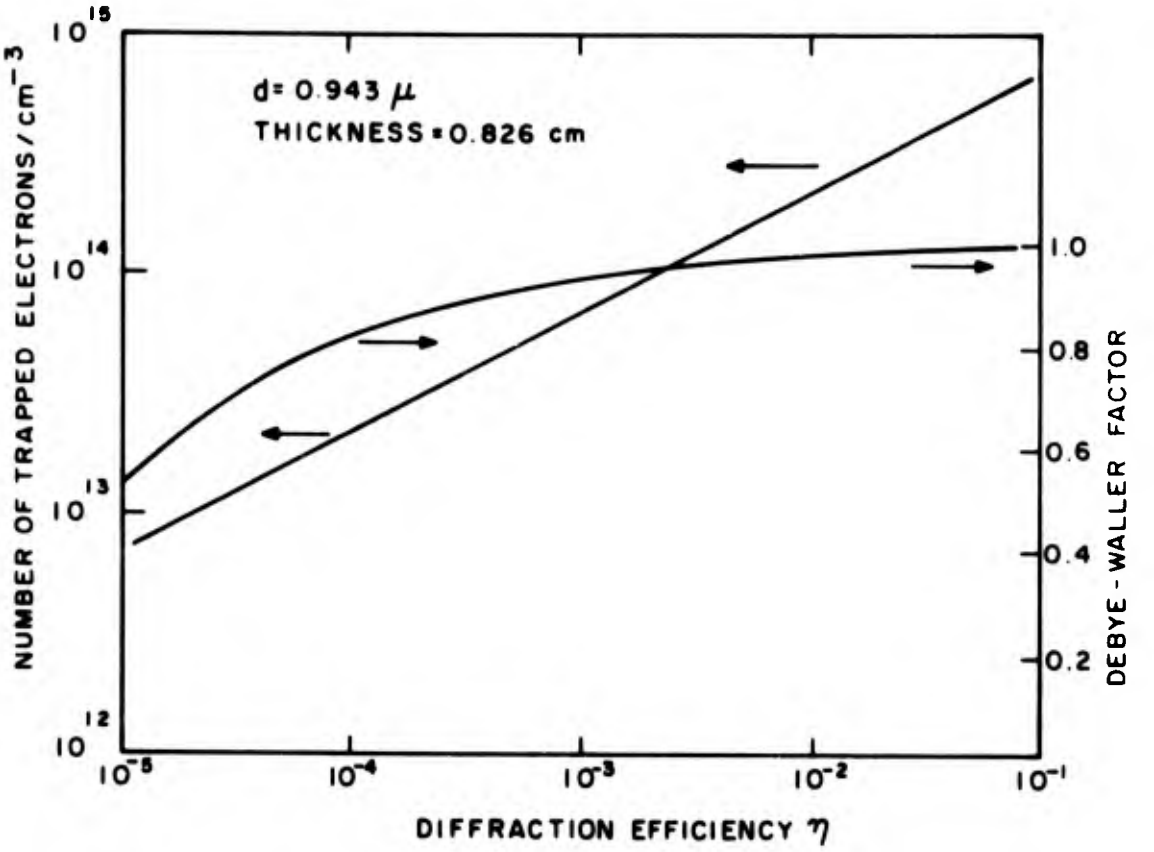

Figure 22. Calculated number of trapped electrons/cm^3 and Debye-Waller correction factor vs diffraction efficiency.

Therefore, for a diffraction efficiency of ∿10%, we can see from Eq. (42) that for such values of the diffraction efficiency the deviation of η_M from η_o is almost nil. Therefore, significant deviations would occur only for much smaller values of diffraction efficiency. Figure 22 shows a plot of the number of trapped electrons/cm^3 and the correction factor plotted vs the diffraction efficiency over the range of interest here. At such small diffraction efficiencies we can approximate η_o as

$$\eta_o = C N^2$$

where C is a proportionality constant. Then we have

$$\eta_M = C N^2 \exp[-2(\pi^2-8)/Nd^3] \qquad (43)$$

Since N is directly proportional to the time of exposure τ, $N = K\tau$ (where K is a constant), we can rewrite Eq. (43) as

$$\ln \eta_M = \text{const.} + 2 \ln \tau - 2(\pi^2-8)/Kd^3 \tau \qquad (44)$$

Equation (44) shows that if $\ln \eta_M$ is plotted against $\ln \tau$, we should get a straight line with slope 2 at large value of τ but should deviate from the straight line at small values of τ.

B. MEASUREMENT

The apparatus used to measure the deviation of the diffraction efficiency from the τ^2 law at low diffraction efficiency is shown in Fig. 23. A 16 line/inch square-wave pattern in photographic emulsion is used as an object. This

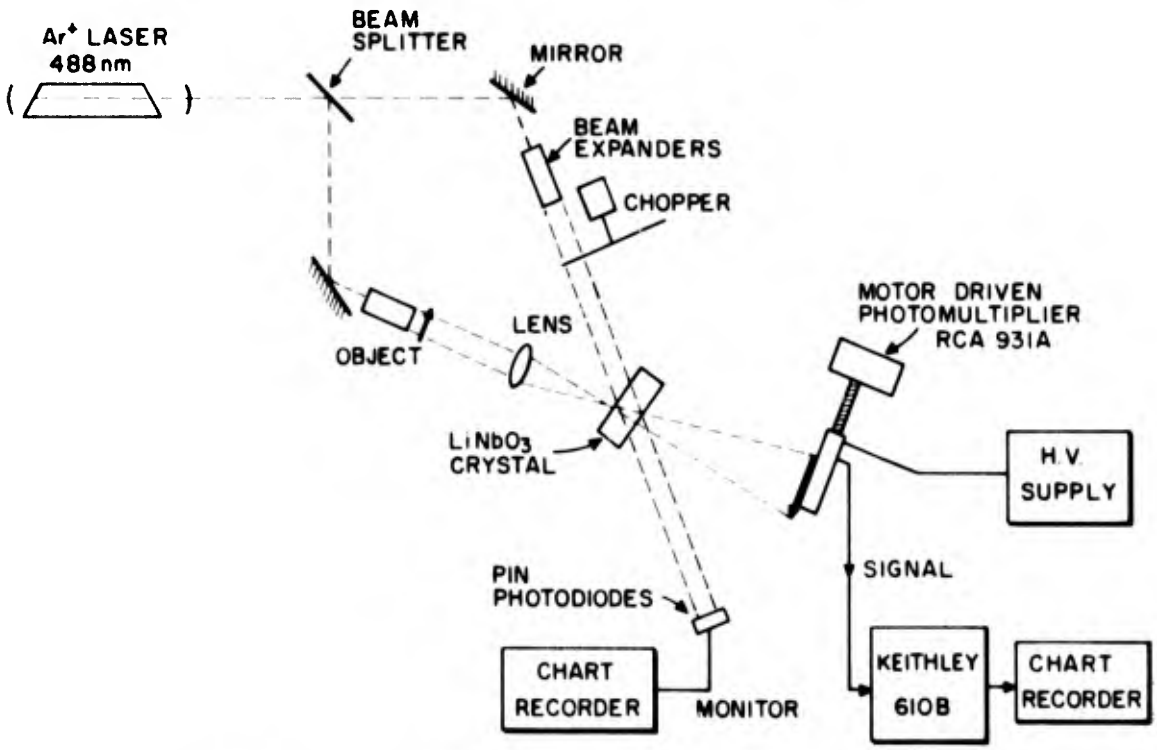

Figure 23. Schematic diagram of the apparatus used to measure statistical noise.

object is imaged at a magnification of ~2X. The readout image of the hologram of this object is then scanned with the photomultiplier tube. The diffracted signal is the difference between the peaks and background of the image. This is shown in Fig. 24.

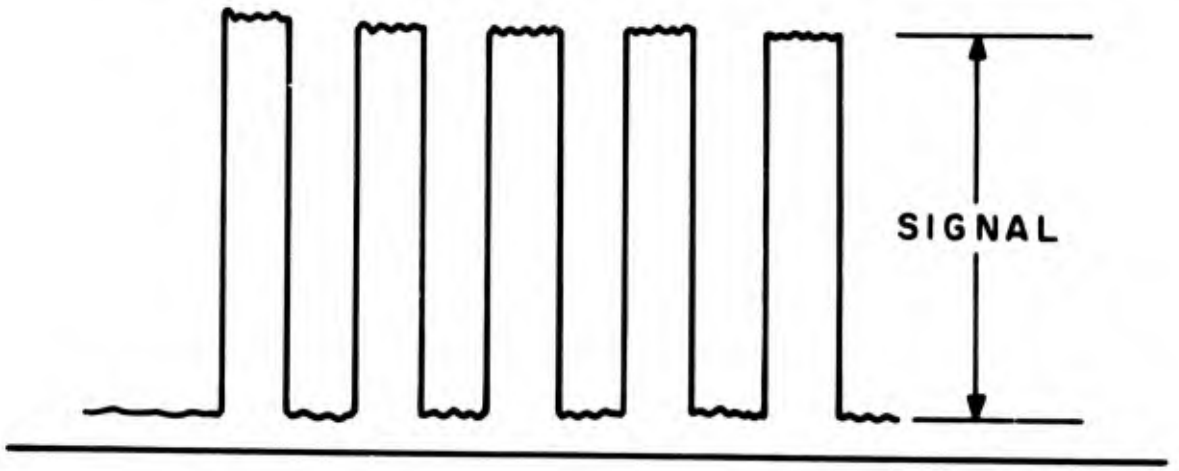

Figure 24. Schematic diagram of signal measured.

The log of the measured diffraction efficiency vs the log of the exposure time is plotted in Fig. 25. The log of the diffraction efficiency is linear in ln τ from $\eta = 5 \times 10^{-5}$ to 5×10^{-3}. The solid line is a least square fit to the data points below $\eta = 6 \times 10^{-3}$.

$$\ln \eta = \ln[(1.73 \pm .35)(10^{-4})] + (1.97 \pm .22) \ln \tau \qquad (45)$$

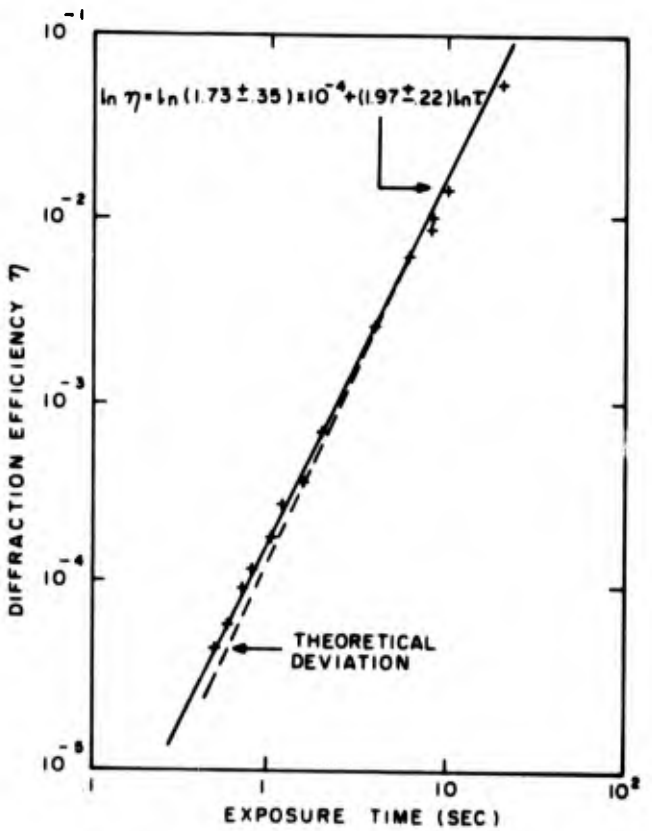

Figure 25. Measured diffraction efficiency vs exposure time for the square-wave pattern imaged onto the detector.

Also shown in Fig. 25 is the calculated value of the deviation from a square law due to the Debye-Waller factor as given in Fig. 22. There is a deviation at the highest diffraction efficiencies from the square law which resembles a saturation effect. It was confirmed that this was not a saturation of the detection system. The breakdown of the $\sin^2\theta = \theta^2$ approximation can only account for $\sim$0.9% of the deviation. There is an additional correction which must also be applied to these data. The lowest diffraction efficiencies were recorded with the crystal approximately normal to the reference beam. After each hologram is recorded and measured, the crystal is rotated $\sim 2°$ to eliminate crosstalk between holograms. As the crystal normal is rotated away from the reference beam the projection of the polarization of the readout beam on the c-axis changes as $\cos\theta$. For the data taken at $\sim$5% diffraction efficiency the change in angle *in the medium* is 16°, which gives an $\sim$8% correction to the diffracted light intensity in the right direction. The remainder of the discrepancy ($\sim$15%) cannot be accounted for at this time.

We also measured this effect using a plane-wave object beam to ensure that the τ^2 law observed above is not an artifact of the optical system. The results are shown in Fig. 26. Again it is clear that at low diffraction efficiencies there is no significant deviation from the τ^2 law. A least squares fit to the data gives

$$\ln \eta = \ln[(5.31 \pm 0.80)\ 10^{-5}] + (1.98 \pm 0.14)\ \ln \tau \qquad (46)$$

Also shown in Fig. 26 is the calculated value of the deviation from a square law due to the Debye-Waller factor as given in Fig. 22. From Figs. 25, 26, and Eq. (44), it is clear that in the range of diffraction efficiencies from 10^{-5} to 10^{-3} the measured curve should deviate significantly from the τ^2 law. In fact, it does not deviate at all in this range and an excellent fit to a square is obtained. The differences in the constant term between the cases shown in Fig. 25 and Fig. 26 are due to different power levels used during recording. The conclusion of these experiments is then that noise arising from granularity in the distribution of trapped electrons which form the grating is insignificant over any conceivable range of diffraction efficiencies in which such holograms would be used.

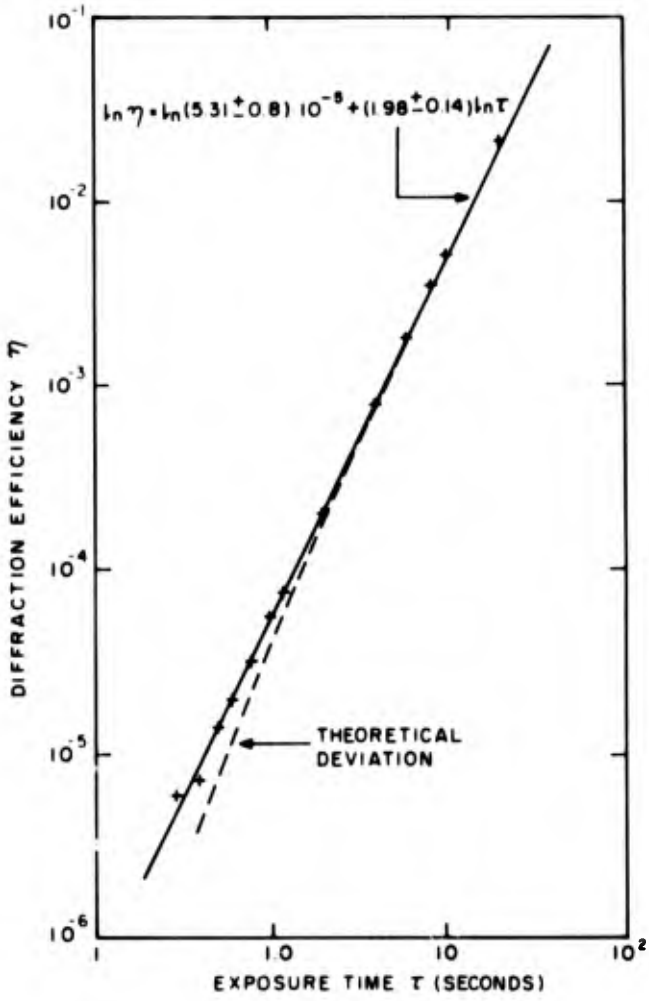

Figure 26. Measured diffraction efficiency vs exposure time for a plane-wave object beam.

The question then arises as to the reason for the discrepancy between the theory and the experiment. A closer examination of the corresponding case for the temperature dependence of the Bragg scattering of x-rays shows that in that case, the structure factor for Bragg scattering is separable into a time-dependent term arising from thermal fluctuations in the position of the scattering ions and a spatial term arising from the equilibrium position of the ions. A thermal average over the time-varying portion produces the Debye-Waller factor.

In the case under consideration here, this fluctuation about the equilibrium position is spatial and not temporal. The vector sum over scattering sites is therefore not separable into equilibrium and fluctuating components, and the exact calculation becomes intractable. However, a Debye-Waller factor

would be expected to give at least an estimate of the magnitude of the effect. The calculation of the Debye-Waller factor presented above shows the effect to be a factor of three less than the estimate of Ramberg [15] and predicts only a factor of $\sim$2 reduction in the readout image at 0.001% diffraction efficiency. Apparently, this estimate is still too large.

VI. SUMMARY AND CONCLUSIONS

We investigated the intrinsic sources of noise present in images read out from volume holograms stored in iron-doped $LiNbO_3$. Three sources of noise were predicted to be present: crosstalk between holograms stored in the same volume, intermodulation distortion, and granularity in the electronic space charge pattern. There are two additional sources of storage medium-related noise present in the readout image. These are: scatter noise due to bulk or surface imperfections in the storage medium itself, and optically induced light scattering.

The magnitude of the crosstalk noise between volume holograms was calculated from Kogelnik's coupled wave theory. These calculations showed that, for thick crystals (>0.4 cm thick), there is no significant increase in the crosstalk noise when more than 50 holograms are stored in a given volume, if the angular spacing is sufficient (>0.1° in air). The magnitude of the crosstalk noise was confirmed by measurements in 0.5- and 0.826-cm-thick-crystals. The measured crosstalk noise from 200 holograms was no different from that for 50 holograms in a 0.826-cm-thick-crystal. Oscillations in the crosstalk S/N ratio corresponding to oscillations in the off-Bragg diffraction efficiency of a single hologram were predicted by the Kogelnik theory and were observed. The periods of these oscillations in the S/N ratio as a function of the angular spacing were larger than predicted, implying that the effective grating thickness is less than the crystal thickness. A measurement of the off-Bragg angular dependence of the intensity of the readout image does not show a corresponding increase in its period of oscillation. This latter effect has been observed by Baugh [17] in films of organic storage media and attributed to variation in grating strength due to absorption of the recording beams as they transit the crystal.

From the results presented in Figs. 7 through 10, it is clear that a S/N ratio due to crosstalk noise of greater than 40 dB can be obtained in crystals whose thickness is greater than 0.5 cm. The oscillatory behavior of S/N ratio will allow larger numbers of holograms to be stored at unexpectedly small angular spacings (e.g., S/N ratio $\tilde{\gtrsim}$ 40 dB for a 0.11° angular spacing in a 0.51-cm-thick crystal). Since an angular spacing in air of $\tilde{\gtrsim}$0.10° is

required in order to store $\gtrsim$500 holograms in a $LiNbO_3$ crystal, it is clear that in excess of 500 holograms can be stored in $LiNbO_3$ crystals greater than 0.5-cm-thick with a crosstalk S/N ratio $\gtrsim$ 40 dB.

The magnitude of intermodulation distortion noise for a two-beam object beam was calculated and measured. The magnitude of the on- and off-Bragg components are strongly suppressed: the on-Bragg IM, because of the small index changes required in thick holograms; the off-Bragg component, because of the Bragg condition for constructive interference. The measured values, while larger than the calculated estimate by 10 to 30 dB, are still small enough that intermodulation will not contribute to any measurable extent to the total noise in any case of practical interest (crystal thickness greater than 0.1 cm).

The magnitude of noise arising from statistical fluctuations in the location of electrons which form the space charge pattern was calculated to be significant only for diffraction efficiencies less than 0.1% in a 0.826-cm-thick crystal. For thinner crystals the magnitude of the effect should be less since a larger index change is required for a given diffraction efficiency. There was, however, no measurable effect arising from this granularity for diffraction efficiencies greater than 0.001%. The reason why this effect is not observable is not clear at present. We can conclude, however, on the basis of these measurements that the statistical fluctuations will not contribute to the observable noise for the range of diffraction efficiencies which would be used in practical applications.

Scatter noise arising from bulk and surface imperfections in the recording medium was measured to be 80 to 100 down from the image intensity for a 10% efficient hologram, and is therefore also insignificant as a noise source. This high S/N ratio is attributable to the excellent optical quality of presently available crystals and the high quality of the surface finish obtainable using SYTON polish.

The development of an SiO_2 antireflection coating for $LiNbO_3$, which is stable during the heating cycles used for fixing and erasing holograms, improved the readout image quality by eliminating multiple reflections in the crystal.

The buildup and angular dependence of optically induced light scattering has been measured previously [19]. In the work reported here a background

light induced scattering of -50 dB was observed when 50 holograms were recorded at room temperature. Previous observations indicate that the buildup of this effect is a highly nonlinear function of the total exposure [19]. This effect is partially suppressed using the record-while-hot technique, since the local space charge field associated with the optical damage during recording is immediately compensated for by ionic motion.

The effect of light-induced optical scattering is primarily seen during prolonged readout of a given hologram. In iron-doped $LiNbO_3$ this effect can be reduced by a combination of several different means: the use of high diffraction efficiency holograms, low laser readout power, high sensitivity image detection (vidicon or light value), and incoherent illumination of the storage medium during readout coupled with a narrow band pass filter suitably located in the readout optics.

An alternative approach for $LiNbO_3$ is the use of other photosensitive dopants which can then be deactivated during readout. Several efforts have been made in this area, but as yet no dopant has been found which approaches iron in sensitivity and thermal stability during fixing.

In summary, noise sources intrinsic to volume phase holograms in iron-doped $LiNbO_3$ have been investigated. Intermodulation distortion, statistical noise, and scatter noise have been found to be insignificant. Crosstalk noise can be reduced to a level compatible with high-quality (S/N ratio $\sim$40 dB) readout images at angular spacings (0.1° in air) such that large numbers of holograms can be stored in a given volume. Light-induced optical scattering during recording and readout can be reduced by proper choices of recording and readout techniques.

REFERENCES

1. P. J. Van Heerden, Appl. Optics 2, 393 (1963).
2. D. L. Staebler, W. Phillips, and B. W. Faughnan, *Materials for Phase Holographic Storage (U)*, Final Report, Contract N00019-72-C-0147, prepared for Naval Air Systems Command, March 1973.
3. D. L. Staebler, W. Phillips, W. Burke and B. W. Faughnan, *Materials for Phase Holographic Storage*, Final Report, Contract No. N00019-73-C-0273, February 1974.
4. W. J. Burke, W. Phillips, D. L. Staebler, and B. F. Williams, *Materials for Phase Holographic Storage*, Final Report, Contract No. N00019-74-C-0312, April 1975.
5. J. J. Amodei, W. Phillips, and D. Staebler, IEEE J. Quantum Electron. QE-7, 63 (1971).
6. G. E. Peterson, A. M. Glass, and T. J. Negran, Appl. Phys. Lett. 19, 130 (1971).
7. F. S. Chen, J. T. LaMacchia, and D. B. Frazer, Appl. Phys. Lett. 13, 233 (1968).
8. D. L. Staebler and J. J. Amodei, J. Appl. Phys. 43, 1042 (1972).
9. J. J. Amodei and D. L. Staebler, Appl. Phys. Lett. 18, 540 (1971).
10. D. L. Staebler and J. J. Amodei, Ferroelectrics 3, 107 (1972).
11. B. F. Williams, W. J. Burke and D. L. Staebler, Appl. Phys. Lett., to be published 15 February 1976.
12. D. L. Staebler, W. J. Burke, W. Phillips and J. J. Amodei, Appl. Phys. Lett. 4, 182 (1975).
13. D. H. R. Vilkomerson, "A Holographic Communication Theory," Ph.D. Thesis, Columbia University (1969).
14. H. J. Gerritsen, W. J. Hannan, and E. G. Ramberg, Appl. Opt. 7, 2301 (1968).
15. E. G. Ramberg, RCA Review 33, 5 (1972).
16. R. A. Bartolini, Applied Optics 13, 129 (1974).
17. R. Baugh, "High Efficiency Volume Holography," (Ph.D. Thesis, Stanford University, 1969).
18. R. G. Zech, "Data Storage in Volume Holograms," (Ph.D. Thesis, University of Michigan, 1974).
19. G. A. Alphonse and W. Phillips, Final Report, Contract No. NAS8-26808, National Aeronautics and Space Administration, May 1975.
20. W. J. Burke, *S/N Ratio of Holographic Images*, Final Report, Contract No. N00019-75-C-0494, November 1975.
21. W. Phillips and D. L. Staebler, J. Elect. Materials 3, 601 (1974).

22. J. J. Amodei, W. J. Burke and D. L. Staebler, *Volume Holographic Materials Characterization and Device Feasibility For Map Display Applications*, Final Report, Contract No. N62269-71-C-0533, July 1972.

23. W. Burke and D. L. Staebler, *Volume Holographic Materials Device Feasibility for Map Display Applications*, Final Report, Contract No. N62269-72-C-0793, June 1973.

24. H. Kogelnik, Bell Syst. Tech. J. 48, 2909 (1969).

25. J. A. Jenney, Appl. Opt. 11, 1371 (1972).

26. C. Kittel, *Introduction to Solid State Physics*, (John Wiley and Sons, Inc., New York, 1971), p. 84.

APPENDIX

In this Appendix we solve the coupled-wave equations, Eqs. (24a) - (24c). The method we use is the Laplace transformation, which converts a set of coupled differential equations into a set of coupled algebraic equations. Let p be the transformation variable and R (p), S_1 (p), S_2 (p), N_1 (p), N_2 (p) be the Laplace transforms of R (y), S_1 (y), S_2 (y), N_1 (y), N_2 (y), respectively. Then the transformed equations are:

$$C_o[pR(p) - 1] = -iK_1S_1(p) - iK_2S_2(p) \tag{A-1}$$

$$C_S\, pS_1(p) + i\vartheta S_1(p) = -iK_1R(p) \tag{A-2}$$

$$C_S\, pS_2(p) + i\vartheta S_2(p) = -iK_2R(p) \tag{A-3}$$

$$C_S\, pN_1(p) - i(\Delta - \vartheta)N_1(p) = -iK_{12}S_1(p) \tag{A-4}$$

$$C_S\, pN_2(p) - i(\Delta - \vartheta)N_2(p) = iK_{12}S_2(p) \tag{A-5}$$

Equations (A-1) - (A-3) can be solved for S_1 (p):

$$S_1(p) = -\frac{iK_1}{C_S}\,\frac{1}{p^2 + (i/C_S)p + [(K_1^2 + K_2^2)/C_oC_S]} \tag{A-6}$$

From Eqs. (A-6) and (A-4) we get N_1 (p):

$$N_1(p) = -\frac{K_1K_{12}}{C_S^2}\,\frac{1}{\left\{p - [i(\Delta - \vartheta)/C_S]\right\}\left\{p^2 + (i\vartheta/C_S)p + [K_1^2 + K_2^2)/C_oC_S]\right\}} \tag{A-7}$$

Performing the inverse Laplace transformation on (A-6) and (A-7), we get

$$S_1(y) = -\frac{iK_1}{C_S}\,\frac{\exp[-i\vartheta y/2C_S]}{\Gamma}\sin \Gamma y \tag{A-8}$$

and

$$N_1(y) = \frac{K_1 K_{12}}{C_S^2} \frac{\exp[-i\vartheta y/2C_S]}{[\Lambda^2 - \Gamma^2]} \quad x$$

$$\left\{[\cos \Lambda y - \cos \Gamma y] + i[\sin \Lambda y - \frac{\Lambda}{\Gamma} \sin \Gamma y]\right\} \qquad \text{(A-9)}$$

where the quantities Λ and Γ have been defined in the text. From Eqs. (A-8) and (A-9), one can directly obtain Eqs. (26) and (29).

DISTRIBUTION LIST

Chief of Naval Research
Vehicle Technology Program
Arlington, Virginia 22217
ATTN: Codes 211 4
427 1
421 1

Defense Documentation Center
Cameron Station
Alexandria, Virginia 22314 12

Director
Naval Research Laboratory
Washington, DC 20375
ATTN: Tech. Info Division 1
Library, Code 2620 1

Director, ONR Branch Office
536 S. Clark Street
Chicago, Illinois 60505 1

Director
Office of Naval Research Branch Office
1030 East Green Street
Pasadena, CA 91106 1

Director
Office of Naval Research Branch Office
495 Summer Street
Boston, Massachusetts 02210 1

Office of Naval Research Branch Office
New York Area Office
715 Broadway (5th Floor)
New York, New York 10003 1

Office of the Secretary of Defense
Deputy Director, Tactical Warfare Program
Washington, DC 20360
ATTN: Dr. Robert Fisher 1

Headquarters
Department of the Navy
Naval Material Command
Washington, DC 20360
ATTN: MAT 03 1

Commander
Naval Air Systems Command
Washington, DC 20360
ATTN: AIR 53351D 1
340D 1
360F 1
03P 1
954 1
310B 4

Commander Naval Sea Systems Command
Code 034
Washington, DC 20360 1

Commander
Naval Electronic Systems Command
Washington, DC 20360
ATTN: ELEX 310 1
320 1

Commanding Officer
U. S. Naval Air
Development Center
Warminster, PA 13974
ATTN: Code 3042 1
544 1

Commander
Naval Electronics Laboratory Center
271 Catalina Boulevard
San Diego, CA 92152 1

Commander
Naval Weapons Center
China Lake, CA 93555
ATTN: Code 4011 1

Commander
Naval Avionics Facility
Indianapolis, Indiana 46218 1

Dean of Research Administration
Naval Postgraduate School
Monterey, CA 93940 4

Commandant, U S Marine Corps
Headquarters, U. S. Marine Corps
Washington, DC 20380
ATTN: RD-1 1

Commandant
U S. Coast Guard Headquarters
400 7th Street, NW
Washington, DC 20591 1

Dir., U. S. Army Research Institute
1300 Wilson Boulevard
Arlington, Virginia 22209 1

Commanding General
U. S. Army Electronics Command
Fort Monmouth, New Jersey
ATTN: AMSEL-VL-E 1
AMSEL-TL-BO 1
AMSEL-VL-I 1

Headquarters AFSC-XRLA
Andrews AFB
Washington, DC 20334 1

Air Force Avionics Laboratory
Air Force Systems Command
Writht-Patterson AFB, Ohio 45433
ATTN: AFAL/AA 1
AFAL/TEL 1

Air Force Flight Dynamics Laboratory
Air Force Systems Command
Wright-Patterson Air Force
Base, Ohio 45433
ATTN: FDCR 1

Headquarters Rome Air Development
Center
Air Force Systems Command
Griffiss Air Force Base, NY 13441
ATTN: RBRAC 1

Advisory Group of Electron Devices
201 Varick St., 9th Floor
New York, NY 10014 1

Federal Aviation Agency
NAFEC Bldg. 10
Atlantic City, NJ 03405 1

Air Force Office of Scientific
Research
1400 Wilson Boulevard
Arlington, Virginia 22209 1

Hughes Aircraft Company
Display Systems & Human Factors
Department
Aerospace Group
Culver City, CA 90230
ATTN: Mr. G. K. Slocum 1

Commanding Officer
Naval Oceanographic Office
Washington Navy Yard, Bldg 160
Washington, DC 20373
ATTN: Mr. C. J. Crandall (Code 6250) 1

Commanding Officer
Air Force Systems Command
Aeronautical Systems Division
Wright-Patterson Air Force Base
Ohio 45433
ATTN; Mr. Guy Lai (ENAC) 1

Defense Mapping Agency
Hydrographic Center, Code PRA
Washington, DC 20390
ATTN: Mr. C. R. Gray 1